Skeletal muscle-restricted expression of human SOD1 causes motor neuron degeneration in transgenic mice

Margaret Wong[1] and Lee J. Martin[1,2,3,*]

[1]Division of Neuropathology, Department of Pathology, [2]Pathobiology Program and [3]Department of Neuroscience, Johns Hopkins University School of Medicine, 558 Ross Building, 720 Rutland Avenue, Baltimore, MD 21205-2196, USA

Amyotrophic lateral sclerosis (ALS) is a fatal neurodegenerative disease of motor neurons (MNs) that causes skeletal muscle paralysis. Familial forms of ALS are linked to mutations in the superoxide dismutase-1 (*SOD1*) gene. The mechanisms of human SOD1 (hSOD1) toxicity to MNs are unknown. We hypothesized that skeletal muscle is a primary site of pathogenesis in ALS that triggers MN degeneration. We created transgenic (tg) mice expressing wild-type-, G37R- and G93A-hSOD1 gene variants only in skeletal muscle. These tg mice developed age-related neurologic and pathologic phenotypes consistent with ALS. Affected mice showed limb weakness and paresis with motor deficits. Skeletal muscles developed severe pathology involving oxidative damage, protein nitration, myofiber cell death and marked neuromuscular junction (NMJ) abnormalities. Spinal MNs developed distal axonopathy and formed ubiquitinated inclusions and degenerated through an apoptotic-like pathway involving capsase-3. Mice expressing wild-type and mutant forms of hSOD1 developed MN pathology. These results demonstrate that human SOD1 in skeletal muscle has a causal role in ALS and identify a new non-autonomous mechanism for MN degeneration explaining their selective vulnerability. The discovery of instigating molecular toxicities or disease progression determinants within skeletal muscle could be very valuable for the development of new effective therapies for the treatment and cure of ALS.

INTRODUCTION

ALS is a progressive, severely disabling fatal neurological disease in humans. The disease is characterized by weakness, muscle atrophy, spasticity and eventual paralysis and death generally within 3 to 5 years after symptoms begin (1). The cause of the spasticity, paralysis and morbidity is progressive degeneration and loss of upper motor neurons (MNs) in cerebral cortex and lower MNs in the brainstem and spinal cord (1,2). The majority of ALS cases are sporadic with no known genetic component, except for missense mutations in TAR-DNA-binding protein (3). Inherited forms of ALS (fALS) have autosomal dominant or autosomal recessive patterns and make up ∼10% or less of all ALS cases (1). Mutations in the superoxide dismutase-1 (*SOD1*) gene account for ∼20% of all fALS cases (∼2% of all ALS cases) (4,5). SOD1 (also known as copper/zinc SOD) is a

metalloenzyme of 153 amino acids (∼16 kDa) that binds one copper ion and one zinc ion per subunit. This enzyme, functioning as a ∼32 kDa non-covalently linked homodimer, is responsible for the detoxification and maintenance of intracellular superoxide anion (O_2^-) concentration in the low femtomolar range by catalyzing the dismutation of O_2^- to molecular oxygen and hydrogen peroxide (6). SOD1 is ubiquitous (intracellular SOD concentrations are typically ∼10–40 μM) in most tissues (7). SOD1 mutants appear to gain a toxic property or function, rather than having diminished O_2^- scavenging activity (4,8,9), and wild-type SOD1 can acquire toxic properties through oxidative modification (10,11).

The triggering events for MN degeneration in ALS are not understood and why MNs are selectively vulnerable is unclear. The extent to which specific intrinsic abnormalities within MNs or within other cells also in the spinal cord

*To whom correspondence should be addressed. Tel: +1 4105025170; Fax: +1 4109559777; Email: martinl@jhmi.edu

contribute to the pathogenesis in models of ALS is discrepant. In transgenic (tg) mice expressing mutant SOD1 (mSOD1) selectively in neurons by a Thy1 promoter, MN degeneration was absent (12,13); however, more recent work shows that neuron-specific expression of human mSOD1 is sufficient to induce MN degeneration in mice (14,15). Tg mice with astrocyte-specific expression of mSOD1 did not develop disease (16), but recent *in vitro* studies reveal that mSOD1 in astrocytes can cause degenerative changes in wild-type MNs and worsen toxicity of mSOD1 in MNs (17). mSOD1 expressed in microglia might also be toxic to MNs in mice (18,19) and in culture (20). Furthermore, degeneration of mSOD1-expressing MNs that are surrounded by wild-type astrocytes or microglia appears delayed or prevented in chimeric mice (21), and transplantation of wild-type neural progenitor cells in the spinal cord of mSOD1 mice delays disease and extends survival (22). However, elimination of proliferating microglia-expressing mSOD1 in mice did not affect MN degeneration (23).

Cells and tissues outside the CNS are diseased in human ALS, including lymphocytes (24), fibroblasts (25,26) and skeletal muscle (27,28). The skeletal muscle pathology and early functional abnormalities occur in human sporadic ALS (29–31) and familial ALS (32,33) and in mSOD1 tg mouse models (34–36), but the abnormalities in skeletal muscle have been interpreted by many investigators to be secondary to the disease mechanisms (30,37,38). Important unresolved questions are the effects of human wild-type and mSOD1 expression specifically in skeletal muscle and the consequences on MNs. Does skeletal muscle itself initiate and contribute to the degeneration of MNs in ALS? We tested the hypothesis that skeletal muscle is a primary site of disease in ALS by creating tg mice with muscle-restricted expression of three different hSOD1 gene variants (hSOD1^{mus}). We found that skeletal muscle abnormalities can initiate the non-autonomous degeneration of MNs in ALS and it can account for the selective vulnerability of MNs in ALS.

RESULTS

tg Mice

We had 22 tg founders for hSOD1^{mus}: 5 were G37R, 2 were G93A and 15 were wild-type. From these founders, we derived 18 hSOD1^{mus} tg lines (2 for G93A, 4 for G37R and 12 for wild-type) identified by PCR. Southern analysis was used to show the presence of transgene. Copy number determined by Southerns ranged from 1 to 25 copies (Fig. 1B). For a more accurate determination of transgene copy number, real-time quantitative PCR (qPCR) was also performed. The copy numbers for lines 25, 112 and 224 determined by Southern analysis were confirmed by qPCR (Fig. 1C).

Western blotting of tissue extracts was done to confirm skeletal muscle-restricted expression of hSOD1 in our tg mice (Fig. 2A). Skeletal muscle-specific expression of hSOD1 was observed in soluble protein fractions (Fig. 2A) and in mitochondria-enriched fractions (Fig. 2B) of tg mice. The level of expression in the soluble protein fraction was ∼5–50% endogenous (Fig. 2A) and in mitochondria-enriched fractions, very low to near-equivalent to endogenous (Fig. 2B), depending on tg mouse line. No hSOD1 protein was detected
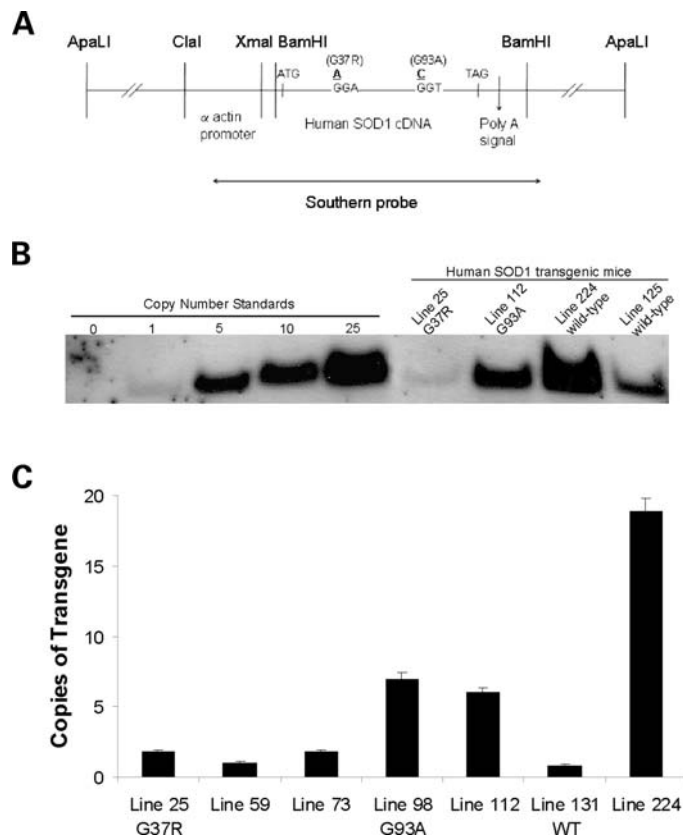
Figure 1. Design of hSOD1^{mus} gene constructs and generation of tg mice. (**A**) Schematic representation of constructs used in creating hSOD1^{mus} mice. The skeletal muscle-specific α-actin promoter was used to drive expression of human wild-type or mSOD1. The human wild-type cDNA is shown. Two different point mutations were introduced by site-specific mutagenesis to convert codon 37 from a glycine to an agrinine or codon 93 from a glycine to an alanine. The probe used for Southern analysis spanned the entire chicken α$_{sk}$ actin promoter and coding region of hSOD1. (**B**) Southern blot analysis of hSOD1^{mus} transgene copy number in different tg mouse lines. *Nco*I digestion of mouse tail genomic DNA yields a 2.5 kb fragment in tg mice. Positive controls/copy number standards were digested tail DNA from non-tg mice spiked with various amounts of *Apa*LI-digested construct. The negative control (0) was non-spiked DNA from non-tg mice. (**C**) qPCR analysis of hSOD1 transgene copy number in representative hSOD1^{mus} tg G37R mice (lines 25, 59 and 73), G93A mice (lines 98 and 112) and wild-type mice (lines 131 and 224). Bars represent mean ± SEM and are the results of triplicate experiments.

in the brain and spinal cord (Fig. 2A) even after using high concentrations of polyclonal primary antibody to hSOD1 and very long exposures. hSOD1 was not found in other tissues analyzed, including the heart, kidney, liver and lung (data not shown). We did not find evidence for stable aggregates of hSOD1 in skeletal muscle of hSOD1^{mus} tg mice at 4–15 months of age.

Although hSOD1 protein was not detected in total spinal cord homogenates of any lines of hSOD1^{mus} tg mice, we nevertheless wanted to rule out the unlikely possibility that hSOD1 is expressed by or incorporated into spinal MNs selectively, perhaps through retrograde transport after uptake from skeletal muscle released at the neuromuscular junction (NMJ). Immunostaining using an hSOD1-specific monoclonal antibody revealed no immunoreactivity in spinal MNs of
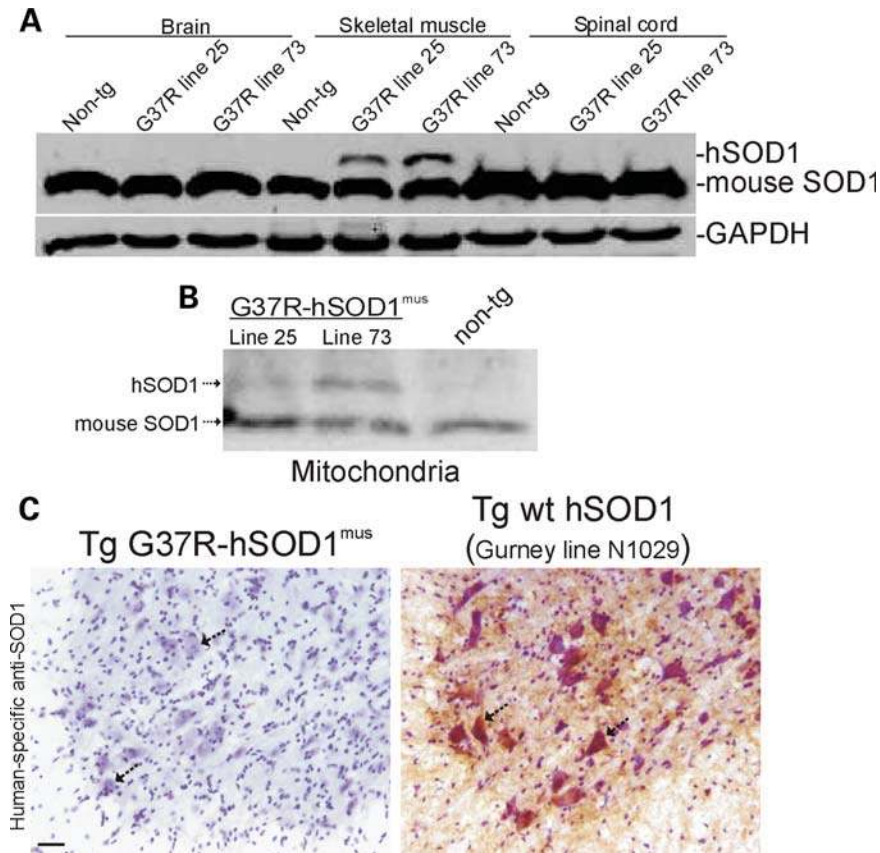
Figure 2. hSOD1^{mus} tg mice express hSOD1 in skeletal muscle but not in CNS. (**A**) Soluble proteins were extracted from hind-leg skeletal muscle, spinal cord and brain of hSOD1^{mus} tg (different mouse lines are identified) and non-tg mice. Samples (100 μg of protein loaded/lane) were electrophoresed in 16% SDS–PAGE gels, electroblotted onto nitrocellulose membrane and immunoblotted using an antibody that binds an epitope common to hSOD1 and mouse SOD1. The blot was re-probed with an antibody to GAPDH as a protein-loading control. (**B**) Proteins from mitochondria-enriched fractions were extracted from hind-leg skeletal muscle (gluteus, biceps and gastrocnemius pooled) and subjected (250 μg of protein) to immunoprecipitation for SOD1 and then western blotting for SOD1. hSOD1 is detected in mitochondria-enriched fractions of hSOD1^{mus} tg mice (two different lines of G37R-hSOD1^{mus} tg mice are shown) but not in non-tg mice. Endogenous (mouse) SOD1 is detected in mitochondria of hSOD1^{mus} tg and non-tg mice. (**C**) Immunohistochemical confirmation that hSOD1 is not present in spinal cord and specifically is not in MNs (arrows) of hSOD1^{mus} tg mice (line 25 is shown). Spinal cord sections were reacted with a mouse mono-clonal antibody specific for hSOD1, and antibody binding was detected using immunoperoxidase with DAB as chromagen (brown reaction product) and counter-stained with CV. Spinal cord sections from tg mice (line N1029, ref. 45) expressing human wild-type SOD1 ubiquitously in a tissue non-specific pattern was a positive control. All spinal MNs in hSOD1^{mus} tg mice are negative (C, left hatched arrows). Most MNs in N1029 mice are strongly positive for hSOD1 (C, right, hatched arrows). Scale bar: 35 μm.

hSOD1^{mus} tg mice (Fig. 2C, left), whereas positive control spinal cord sections showed intensely immunoreactive MNs (Fig. 2C, right).

hSOD1^{mus} tg mice have a neurologic phenotype

hSOD1^{mus} tg mice develop apparently normal neurologically with respect to size, posture, gait and exploratory behavior. However, they develop a complex age-related, abnormal motor syndrome. At 8–10 months of age, mutant hSOD1^{mus} tg mice begin to show a neurologic phenotype (Fig. 3). It consists of spasticity, hyper-flexion and clasping of the hind limbs or forelimbs when dangled by the tail (Fig. 3B), whereas non-tg age-matched littermates typically showed extension of limbs and splaying of digits (Fig. 3A). Neurologic disease in these mice presents initially unilaterally and then becomes bilateral and can involve all four limbs. Older mutant

hSOD1^{mus} tg mice (12–15 months) showed a pronounced paresis of the hind feet with the inability to extend the legs to assume a broad posture for climbing a wire incline and inability to grasp (Fig. 3D), whereas age-matched non-tg mice easily negotiated the same task. Wild-type hSOD1^{mus} tg mice had a more variable overt neurologic phenotype compared with mutant hSOD1^{mus} tg mice. Quantitative assessment of motor activity on a running wheel test revealed significant deficits in mutant and wild-type hSOD1^{mus} tg mice compared with age-matched controls (Fig. 3E and F). Mutant and wild-type hSOD1^{mus} tg mice had significantly lower activity on the running wheel at 10–14 months of age compared with age-matched non-tg mice (Fig. 3E). Mutant and wild-type hSOD1^{mus} tg mice were also significantly weaker than age-matched controls as revealed by their strength on the wire hang-time test (Fig. 3F). However, a lifespan-shortening effects in hSOD1^{mus} tg mice showed low penetrance.
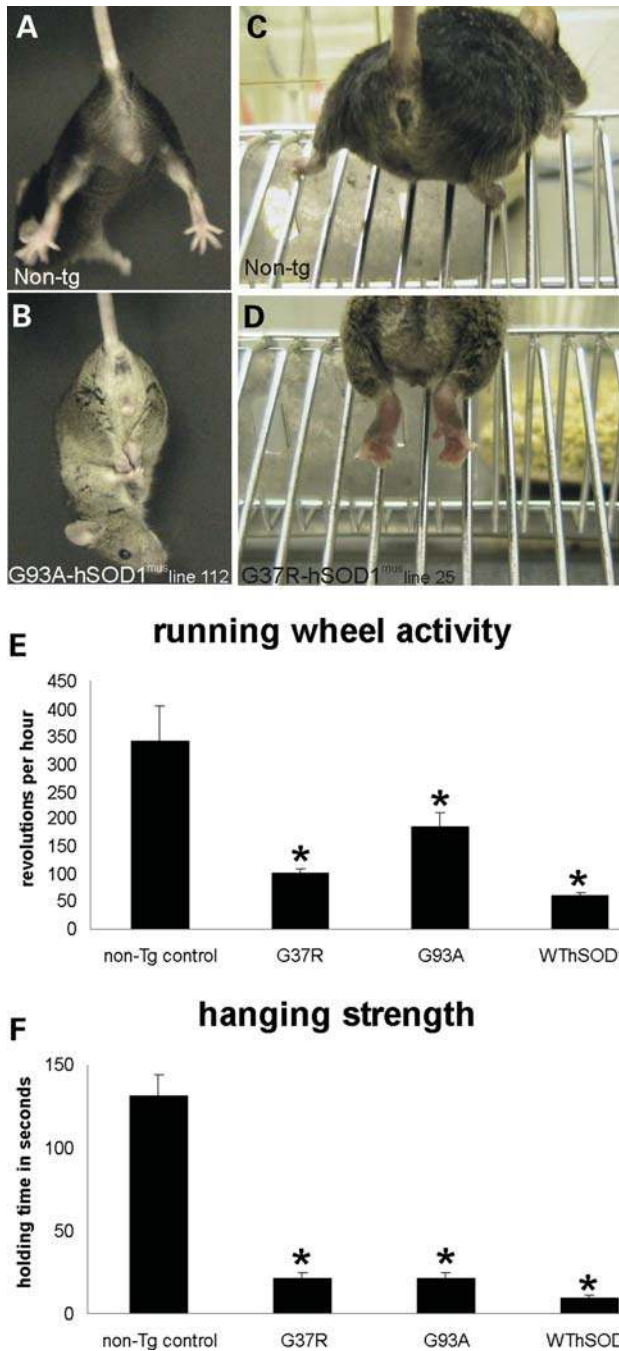
Figure 3. hSOD1^mus tg mice develop weakness and abnormalities in motor function. (**A** and **B**) Normal non-tg mice extend their hind legs and splay their digits (A) when lifted by the tail, whereas age-matched hSOD1^mus tg mice (8–10 months old, line 112) are weak and cannot extend their hind legs or forelimbs (B). (**C** and **D**) When climbing on a steel wire incline, normal non-tg mice assume a broad gait and grip the bars with their paws, whereas age-matched hSOD1^mus tg mice (12–15 months old, line 25) cannot extend their legs, and their paws are unable to grip the bars. (**E**) hSOD1^mus tg mice expressing mSOD1 variants have significantly decreased activity in a running wheel compared with age-matched non-tg mice. Values are mean $\pm$ SEM (different lines for each construct are grouped). Asterisk indicates significant difference ($P < 0.05$) from control. (**F**) hSOD1^mus tg mice expressing mutant and wild-type hSOD1 variants have significantly decreased ability to hang from a wire compared with age-matched non-tg mice. Values are mean $\pm$ SEM (different lines for each construct are grouped). Asterisk indicates significant difference ($P < 0.05$) from control.

hSOD1^mus tg mice develop skeletal muscle pathology

Forelimb (triceps) and hind-limb (gluteus, biceps and gastrocnemius) skeletal muscle in asymptomatic and symptomatic mutant and wild-type hSOD1^mus tg mice had myopathy that was not seen in age-matched non-tg mice (Fig. 4). In control skeletal muscle seen in hematoxylin and eosin (H&E)-stained transverse sections, the myofibers are grouped as polygonal, evenly pink cells with peripherally located nuclei, and there is minimal intervening connective tissue among the myofiber groups (Fig. 4A). In contrast, in similar H&E-stained transverse sections, the skeletal muscle in tg mice displayed shrunken myofibers that converted from polygonal to round in shape with the presence of intramyofiber nuclei, and there was infiltration of loose connective tissue between the myofibers (Fig. 4B). Counting individual myofibers in cross-sections of gastrocnemius muscle revealed a significant loss of myofibers in mutant hSOD1^mus tg (Fig. 4C). The loss of myofiber number was due to death of myofibers as demonstrated by *in situ* detection of nuclear DNA fragmentation by terminal deoxnucleotidyl tranferase dUTP nick-end labeling (TUNEL) of nuclei in individual myofibers (Fig. 4D, arrow). H&E-stained skeletal muscle sections cut in longitudinal profile revealed findings similar to those seen in cross-section (Supplementary Material, Fig. S1). The mostly straight and uniform arrangement of myofibers seen in non-tg mice (Supplementary Material, Fig. S1A) was converted to highly irregular and pale myofibers in tg mice (Supplementary Material, Fig. S1B). Within these diseased foci, the muscle cells showed a homogenizing cell injury characterized by replacement of the normal striated appearance seen in controls (Supplementary Material, Fig. S1A, inset) with diffuse amorphous eosinophilic staining, indicative of sarcolysis of individual myofibers in tg mice (Supplementary Material, Fig. S1B, inset).
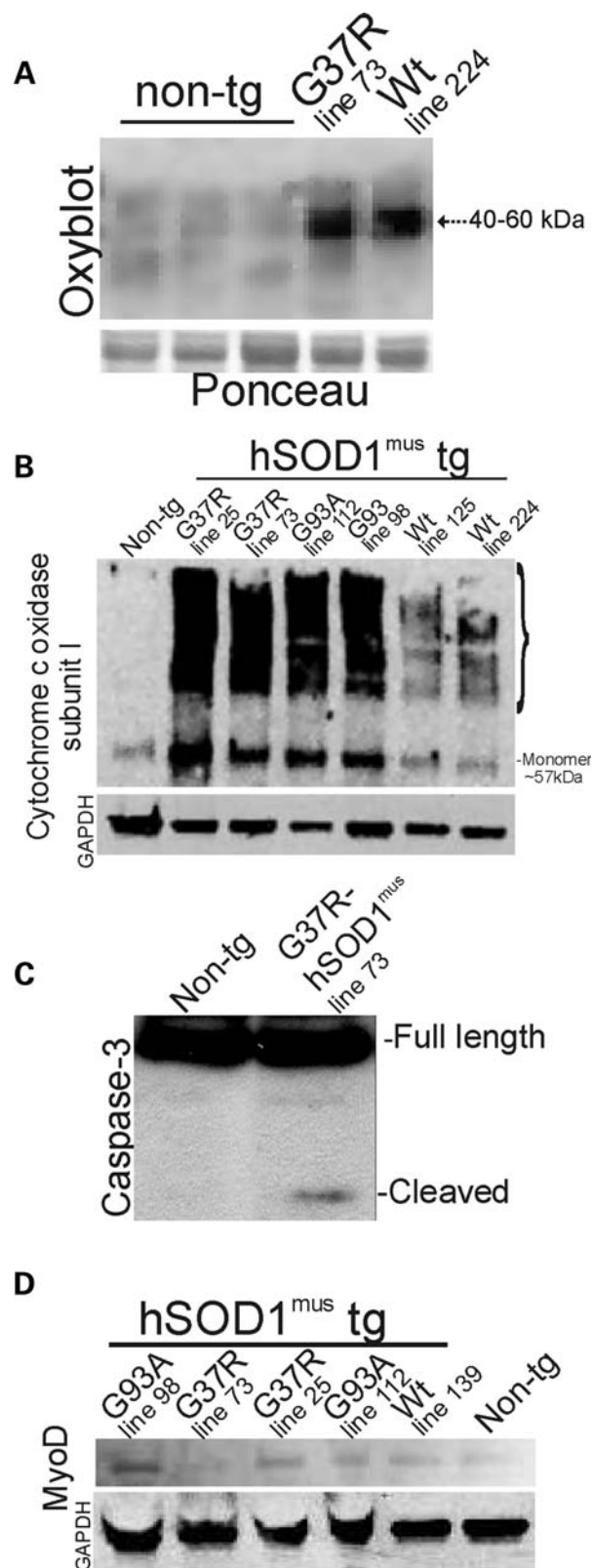
Histochemical staining for ATPase and cytochrome c oxidase (Cox), to distinguish between fast type-1 fibers and slow type-2 fibers, was used to corroborate skeletal muscle pathology in hSOD1^mus tg mice seen by H&E staining. In non-tg controls, occasional intensely high ATPase (pH 9.6)-positive myofibers are seen distributed among more numerous myofibers with moderate ATPase activity (Fig. 4E, arrows). In hSOD1^mus tg mice, ATPase (pH 9.6)-positive myofibers with highest intensity are lost and there is attenuation of enzyme activity in the myofiber majority (Fig. 4F). Cox histochemistry revealed in non-tg mouse skeletal muscle the subset of moderately stained mitochondrial active fast-twitch myofibers among a majority of myofibers with low Cox activity (Fig. 4G, arrows). Skeletal muscle in hSOD1^mus tg mice showed much greater overall staining than in non-tg mice (Fig. 4H compared with 4G), and subsets of myofibers showed very high levels of Cox activity (Fig. 4H, arrows). There was an increased proportion of myofibers with high Cox activity relative to the total population of myofibers (Fig. 4H). Skeletal muscle sections from non-tg and hSOD1^mus tg mice cut in longitudinal profile and stained for Cox activity showed patterns similar to those seen in cross-section (Supplementary Material, Fig. S1C and D).

Oxidative modification of proteins was assessed in hind-limb skeletal muscle (gluteus, biceps and gastrocnemius pooled) of G37R- and wt-hSOD1^mus tg mice using an OxyBlot for carbonyl groups (aldehydes and ketones).
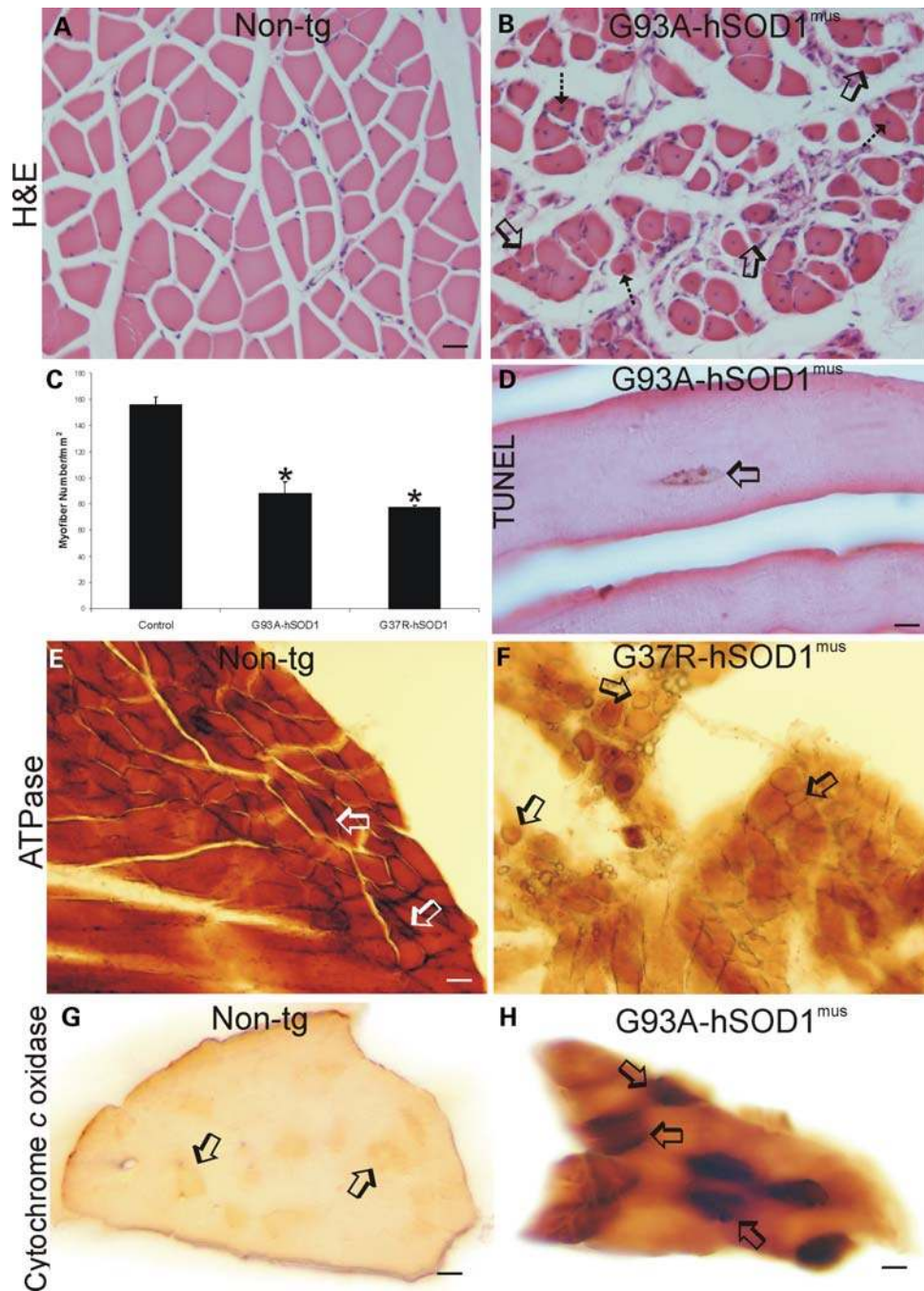
Figure 4. hSOD1[mus] tg mice develop severe myopathy and myofiber cell death. (**A**) Transverse H&E-stained sections of gastrocnemius in 12-month-old non-tg mice show that myofibers are stained homogeneously with eosin and have peripherally located hematoxylin (blue)-stained nuclei. The individual myofibers are plump and polygonal or triangular. (**B**) Transverse H&E-stained sections of gastrocnemius in age-matched hSOD1[mus] tg mice (G93A, line 98 is shown) have degenerating skeletal muscle. The myofibers are round and shrunk (open arrows) or are irregular in shape and have centrally located nuclei (hatched arrow). Loose, irregularly arranged connective tissue infiltrates into the skeletal muscle. Scale bar (A and B): 47.5 µm. (**C**) The graph of gastrocnemius myofiber counts in 10–15-month-old non-tg and mutant hSOD1[mus] tg mice (different lines for each construct are grouped) as determined from transverse H&E-stained sections. Values are mean ± SEM. Asterisk indicates significant difference ($P < 0.05$) from control. (**D**) TUNEL revealed myofiber nuclear DNA fragmentation (brown nucleus, open arrow), indicating cell death, in hSOD1[mus] tg mice (line 98 is shown). Scale bar: 16 µm. (**E** and **F**) Enzyme histochemical staining for myofiber ATPase in non-tg mice skeletal muscle (biceps) revealed a pattern of darkly stained type-1 fibers (open arrows) and more moderately stained type-2 fibers (E), whereas ATPase staining of hSOD1[mus] tg mouse skeletal muscle (line 25 is shown) revealed a loss of type-1 fiber staining and the presence of grouped atrophy (arrows). Sections shown from different mice were incubated at the same time under identical conditions. Scale bar (E and F): 34 µm. (**G** and **H**) Enzyme histochemical staining for Cox activity (brown labeling) in transverse sections of gastrocnemius muscle of age-matched non-tg mice and hSOD1[mus] tg mice (line 112 is shown) revealed differences in mitochondrial oxidative metabolism. In 12–15-month-old non-tg mouse skeletal muscle, some myofibers (arrows) stain more darkly than the myofiber majority, whereas in hSOD1[mus] tg mice (line 112 is shown), most myofibers stain more darkly than control, and a subset of myofibers shows very high enzyme activity (H, arrows). Sections shown from different mice were incubated at the same time under identical conditions. Scale bars: 44 µm (G); 22 µm (H).

Oxidative damage to proteins in the mitochondria-enriched fraction was considerable in 2–4-month-old hSOD1^{mus} tg mice expressing mutant and wild-type hSOD1 (Fig. 5A). Proteins at the size of 40–60 kDa were prominent targets of oxidative damage.
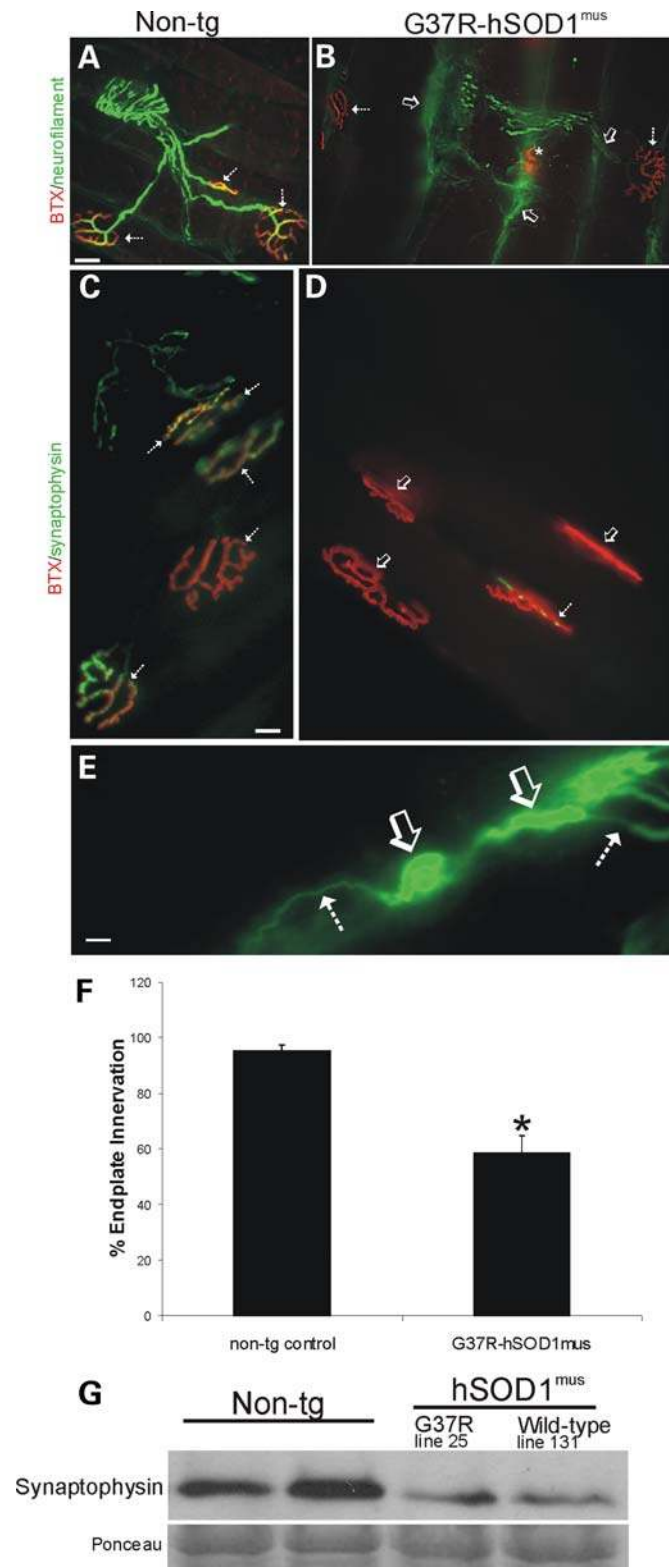
Western blotting for Cox subunit I (Cox-I) revealed two robust findings in mitochondria-enriched fractions of mutant hSOD1^{mus} tg mouse skeletal muscle (gluteus, biceps and gastrocnemius muscles pooled). First, Cox-I protein monomer was elevated prominently in mutant hSOD1^{mus} tg mice (but much less in wild-type hSOD1^{mus} tg mice) compared with age-matched non-tg mice (Fig. 5B). Second, mutant and wild-type hSOD1^{mus} tg mice had formed stable higher molecular weight species of Cox-I (Fig. 5B).

Nitration of proteins was assessed in skeletal muscle of hSOD1^{mus} tg mice by western blotting for 3-nitrotyrosine (Supplementary Material, Fig. S2A). Both mitochondria-enriched and soluble fractions of skeletal muscle from G37R, G93A and wild-type hSOD1^{mus} tg mice had age-dependent and gender-dependent changes in protein nitration. Male mice at ~1.5 years of age had 2-fold elevations in nitrated proteins in both mitochondrial and soluble fractions (Supplementary Material, Fig. S2B), and at ~2 years of age, the fold elevation was less (Supplementary Material, Fig. S2B). In contrast, female mice at ~1.5 years of age had >2-fold elevations in nitrated proteins only in mitochondrial protein (Supplementary Material, Fig. S2C), and at ~2 years of age, protein nitration was significantly lower than age-matched controls (Supplementary Material, Fig. S2C).

Immunoblots of skeletal muscle in mutant hSOD1^{mus} tg mice revealed caspase-3 activation, as indicated by the formation of the cleaved subunit (Fig. 5C), compared with age-matched non-tg muscle.

To examine whether some of the hyper-cellularity seen in skeletal muscle of hSOD1^{mus} tg mice represents regenerative activity, western blots of skeletal muscle nuclear extracts were performed for the satellite-stem cell marker MyoD. MyoD was elevated in both wild-type and mutant hSOD1^{mus} tg mice (and less so in wt hSOD1^{mus} tg mice) compared with age-matched non-tg mice (Fig. 5D).

Figure 5. Immunoblots confirm histological evidence of degenerative changes in skeletal muscle of hSOD1^{mus} tg mice and show evidence for regenerative changes. (**A**) OxyBlot for carbonyl-modified proteins in the mitochondria-enriched fraction of 2–4-month-old non-tg and hSOD1^{mus} tg mice. Tg mice expressing mutant and wild-type (Wt) variants of hSOD1, lines 73 and 224, respectively, have increased oxidative damage to proteins compared with controls. The same blot was stained with Ponceau S to show protein loading. (**B**) Western blot for Cox-I in the mitochondria-enriched fraction (5 µg of protein per lane) of 2–4-month-old non-tg and hSOD1^{mus} tg mice. In non-tg mice, Cox-I is detected primarily as a monomer at ~57 kDa (far left lane). The levels are elevated, and numerous higher molecular weight forms of Cox-I are formed in hSOD1^{mus} tg mice expressing G37R mutant (lines 25 and 73) and G93A mutant (lines 112 and 98). hSOD1^{mus} tg mice expressing wild-type hSOD1 (lines 125 and 224) also showed higher molecular weight species of Cox-I. The blot was re-probed for GAPDH as a protein-loading control. One G93A lane was underloaded. (**C**) Western blot for caspase-3 in the soluble protein fraction (100 µg of protein per lane) of skeletal muscle of 2–4-month-old non-tg and hSOD1^{mus} tg mice. Cleaved subunit was detected in G37R-hSOD1^{mus} tg mice (line 73). Full-length pro-enzyme, but not the cleaved subunit, was detected in age-matched non-tg mice. (**D**) Western blot for MyoD in the nuclear-enriched fraction (50 µg of protein per lane) of 2–4-month-old non-tg and hSOD1^{mus} tg mice. MyoD levels are elevated in G37R mutants (lines 73 and 25), G93A mutants (lines 98 and 112) and wild-type (Wt, line 139) hSOD1^{mus} tg mice compared with non-tg mice. The blot was re-probed for GAPDH as a protein-loading control.

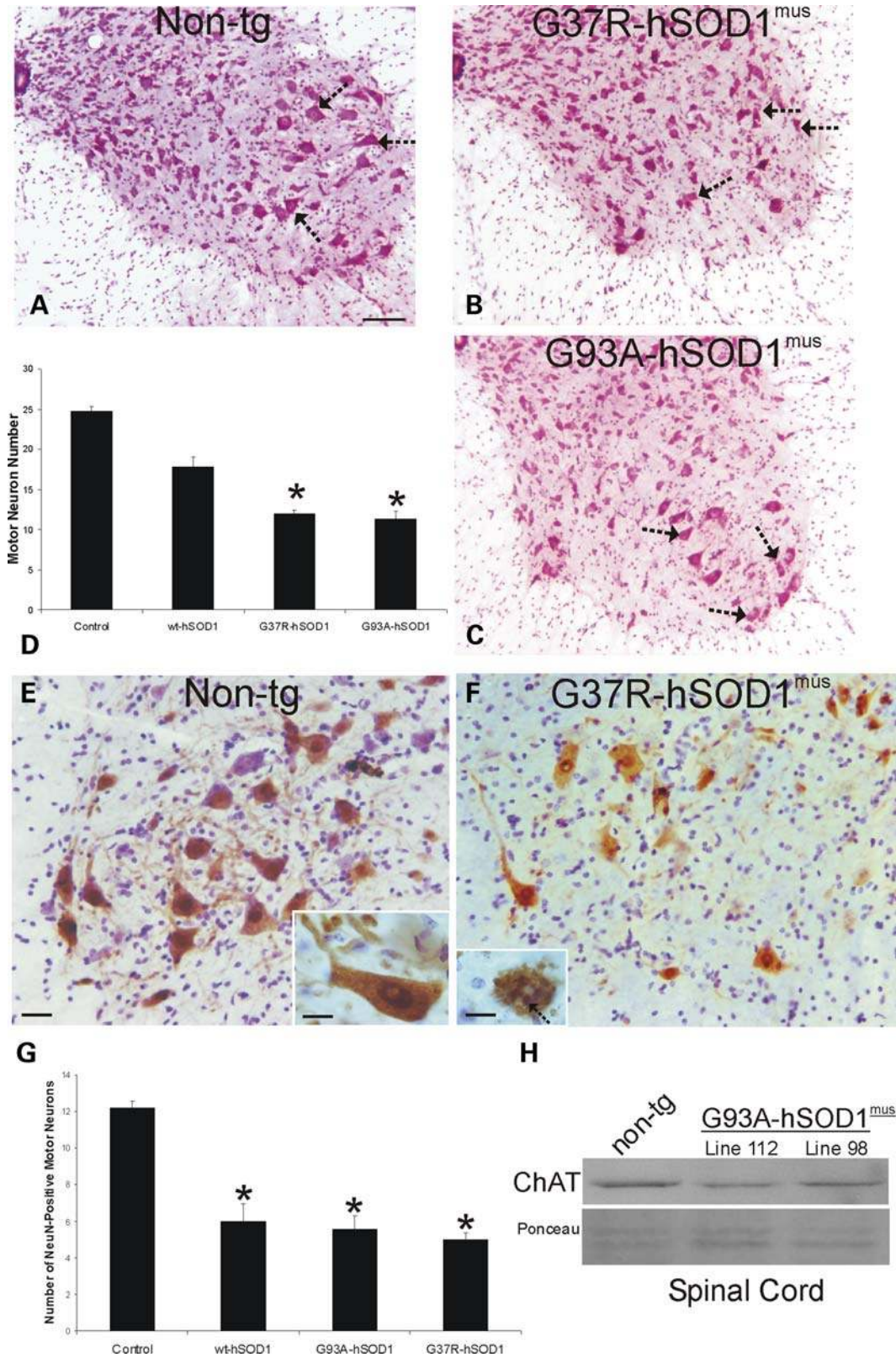## hSOD1^mus tg mice develop NMJ abnormalities and MN distal axonopathy

In non-tg mice, the MN distal axons were smooth and uniform in caliber, and motor endplates appeared as round or elliptical plaque-like arrangements of tubular junctional folds when visualized with fluorescent-conjugated α-bungarotoxin (BTX) (Fig. 6A and C). MN axons innervated motor endplates precisely in control mice (Fig. 6A) with near-100% occupancy (Fig. 6F).

hSOD1^mus tg mice had abnormalities in MN distal axons and motor endplates in forelimb (triceps) and hind-limb (gluteus, biceps and gastrocnemius) skeletal muscles. In mutant hSOD1^mus tg mice, many MN axons were swollen or vacuolated and others ended as bulbs with numerous neurites (Fig. 6B), possibly in part representing compensatory sprouting as seen in other models (39). Some motor endplates were small, collapsed and condensed (Fig. 6B). These were seen only occasionally in non-tg mice, but damaged endplates in mutant hSOD1^mus tg mice were seen frequently. Wild-type hSOD1^mus tg mice also had a higher percentage of endplates that were damaged compared with age-matched controls. The innervation of motor endplates in gluteus and biceps muscles by MN axon terminals was scored as innervated or denervated. Mutant hSOD1^mus tg mice had an ∼40% loss of endplate innervation compared with age-matched controls (Fig. 6F). We used western blotting for synaptophysin in skeletal muscle (gluteus, biceps and gastrocnemius pooled) extracts to confirm the histologic evidence for NMJ damage in hSOD1^mus tg mice. Mutant and wild-type hSOD1^mus tg mice showed very prominent reductions (∼75% loss) in skeletal muscle synaptophysin immunoreactivity compared with age-matched non-tg controls (Fig. 6G).

Mutant hSOD1^mus tg mice developed extensive and conspicuous axonal degeneration in intramuscular peripheral nerve (Fig. 6E). Subsets of axons in peripheral nerve were enlarged,

complete occupancy of motor endplates with MN axons (A, hatched arrows). By 12 months of age, mutant hSOD1^mus tg mice (line 25 is shown) had highly irregular shaped (dystrophic) MN distal axons (B, arrow), some of which were swollen and with apparent sprouts, and motor endplates were denervated (B, open arrows). Some (∼33%) of the motor endplates in hSOD1^mus tg mice appeared small and collapsed (B, asterisk). Scale bar (A and B): 25 μm. (**C** and **D**) Hind-leg skeletal muscle (gluteus, biceps femoris and medial gastrocnemius muscles) was dual-labeled with antibody to synaptophysin (green) and BTX-Texas Red to identify MN pre-synaptic bouton innervation of motor endplates in age-matched non-tg mice and hSOD1^mus tg mice. Control mice had richly ramifying pre-synaptic axon terminals with precise, near-complete innervation of the motor endplates (C, hatched arrows, yellow). In mutant hSOD1^mus tg mice (line 25 is shown), many motor endplates lacked pre-synaptic innervation (D, open arrows) or were only sparsely innervated by MN axon boutons (D, hatched arrow). Scale bar (C and D): 20 μm. (**E**) Intramuscular axon in G37R- hSOD1^mus tg mouse (line 25) showing axonopathy as seen by swollen and tortuous segments (open arrow) interspersed between normal segments of axon (hatched arrows). Scale bar: 10 μm. (**F**) Graph showing counts of the number of motor axon-innervated endplates in medial gastrocnemius muscle of mutant hSOD1^mus tg mice (all G37R lines are grouped). Values are mean ± SEM, $n = 3$–6 mice per group. Asterisk denotes significant difference ($P < 0.05$) from control. (**G**) Western blot for the pre-synaptic vesicle protein synaptophysin in skeletal muscle extracts of age-matched (12–15 months) non-tg mice and hSOD1^mus tg mice expressing G37R (line 25) or wild-type (line 131) variants. Equivalent protein loading is shown by the Ponceau S-stained membrane.

Figure 6. hSOD1^mus tg mice develop NMJ abnormalities, including loss of endplate occupancy, axonopathy and loss of pre-synaptic terminals. (**A** and **B**) Hind-leg skeletal muscle (gluteus, biceps femoris and medial gastrocnemius muscles) was dual-labeled with antibody to neurofilament (green) and BTX-conjugated Texas Red to identify MN axon innervation of motor endplates in age-matched non-tg mice and hSOD1^mus tg mice. Control mice had normal appearing MN distal axons with uniform morphology and nearly

Figure 7. hSOD1[mus] tg mice expressing mutant variants have loss of spinal MNs at ∼1 year of age. (**A–C**) Images of lumbar spinal cord sections stained with CV (hemisections are shown) representative of non-tg (A) and hSOD1[mus] tg mice expressing G37R (B, line 25) and G93A (C, line 112) mutants. Depletion of some MNs (arrows) is evident in G37R and G93A mice. Scale bar (A–C): 100 μm. (**D**) Graph of lumbar MN numbers in control non-tg mice and hSOD1[mus] tg mice expressing wild-type and mutant hSOD1 (different lines for each construct are grouped). Values are mean ± SEM. G37R and G93A mice have a significant loss ($P < 0.05$) of MNs. (**E**) Immunohistochemistry shows that large multipolar α-MNs in the ventral horn of non-tg mice are positive for the DNA-binding

swollen, distorted and vacuolated. These abnormalities were not evident in age-matched non-tg littermate control mice.

hSOD1^{mus} tg mice have degeneration of MNs

We analyzed six lines of hSOD1^{mus} tg mice and age-matched non-tg control mice for spinal cord pathology with Nissl and silver staining as well as immunohistochemical staining for the neuronal DNA-binding protein NeuN, manganese superoxide dismutase (MnSOD) as a mitochondrial marker, neurofilament, ubiquitin, microtubule-associated protein-2 (MAP2) and glial fibrillary acidic protein (GFAP). A conspicuous feature seen by Nissl staining of spinal cord sections of mutant hSOD1^{mus} tg mice was MN loss at 10–15 months of age (Fig. 7B and C) compared with the very visible MNs seen in age-matched controls (Fig. 7A). Cell counting detected significant losses (∼50%) of MNs in lumbar and cervical spinal cord in mutant hSOD1^{mus} tg mice and less MN loss (∼25%) in wild-type hSOD1^{mus} tg mice (Fig. 7D). To corroborate that the large α-MNs were reduced in number, we immunolabeled lumbar spinal cord sections for NeuN (Fig. 7E and F), which distinguishes α-MNs from γ-MNs in the spinal cord (40). NeuN is expressed robustly in the nucleus and in the cytoplasm of large multipolar α-MNs (Fig. 7E, inset). All lines of mutant and wild-type hSOD1^{mus} tg mice analyzed consistently had 50–60% fewer NeuN-positive α-MNs than age-matched non-tg controls (Fig. 7G). Moreover, in hSOD1^{mus} tg mice, some remaining NeuN-positive α-MNs converted from a large multipolar morphology to a shrunken and round morphology and had disintegrating nuclei with round NeuN-positive fragments (Fig. 7F, inset, arrow), features consistent with neuronal apoptosis (41). Because mouse spinal MNs are cholinergic, we also used western blotting for choline acetyl transferase (ChAT) in spinal cord extracts to confirm the histological evidence for MN loss in hSOD1^{mus} tg mice. Mutant hSOD1^{mus} tg mice showed very prominent reductions (∼50% loss) in the spinal cord ChAT immunoreactivity compared with age-matched non-tg controls (Fig. 7H).

MNs in 10–15-month-old G37R-, G93A- and wt-hSOD1^{mus} tg mice showed (Fig. 8B–D) somatodendritic attrition, cytoplasmic microvacuolation, cytoplasmic inclusions (Fig. 8B, D and E), nuclear shrinkage (Fig. 8B–D, asterisks) and clumping of chromatin (Fig. 8B–D, asterisks). In contrast, individual MNs in age-matched non-tg control mice had a large open nucleus with a prominent nucleolus (Fig. 8A, asterisk) and broad proximal dendrites (Fig. 8A, open arrow). To assess the somatodendritic attrition directly and quantitatively, the cell body volumes of individual MNs in lumbar spinal cord were measured in Nissl-stained sections. In controls, average MN cell body volume was ∼25 000 μm^3 (Fig. 8F), which is consistent with other studies (42). In contrast, remaining MNs in G37R-, G93A- and wt-hSOD1^{mus} tg mice were generally less than half of normal MN volume (Fig. 8F). Intra-neuronal, round cytoplasmic inclusions were found in the cytoplasm of some MNs of mutant hSOD1^{mus} tg mice (Fig. 8B and D, hatched arrow), and some intracytoplasmic inclusions in MNs were positive for ubiquitin (Fig. 8E, asterisk). Since mitochondrial swelling contributes to the cytoplasmic microvacuolation of spinal MNs in other tg mice expressing G93A-hSOD1 (43,44), we characterized the cytoplasmic microvacuolation of MNs in G37R-, G93A- and wt-hSOD1^{mus} tg mice by immunolabeling mitochondria with antibody to MnSOD. In control mice, MnSOD immunoreactivity is seen as discrete particles within the cytoplasm and proximal dendrites of MNs (Fig. 8G, hatched arrow). Measurement of the diameter of individual mitochondria within MN cell bodies revealed an average mitochondrial diameter of ∼1 μm in controls (Fig. 8H). MNs in G37R-, G93A- and wt-hSOD1^{mus} tg mice had mitochondria that were smaller (Fig. 8I and H) and were more numerous (Fig. 8I and J) than MNs of age-matched controls (Fig. 8G, H and J).

To examine further the magnitude of MN somatodendritic attrition as well as the potential axonal pathology, we immunolabeled hSOD1^{mus} tg and non-tg mouse spinal cord sections for two very different neuron-specific cytoskeletal proteins, MAP2 and neurofilament. In non-tg mice, MAP2 immunoreactivity is highly enriched in the spinal cord ventral horn where it is present in MN cell bodies (Fig. 9A, arrow) and is concentrated in the neuropil where it represents the dendritic meshwork (Fig. 9A). The spinal cord ventral horns in 10–15-month-old G37R-, G93A- and wt-hSOD1^{mus} tg mice showed significant loss of MAP2 immunoreactivity (Fig. 9B and C), and some individual MN cell bodies were found shrunken without dendrites or with attritional dendrites (Fig. 9B, arrows). In sections stained for phosphorylated neurofilament, MN cell bodies in control mice show low cytoplasmic immunoreactivity (Fig. 9D); in contrast, subsets of MNs in hSOD1^{mus} tg mice accumulated phosphorylated neurofilament protein in shrunken cell bodies (Fig. 9E, arrows). Prominent axonal abnormalities (large swollen or distended and tortuous) and degeneration were seen in hSOD1^{mus} tg mouse spinal cord sections stained by neurofilament antibody (Fig. 9F, arrows). Normal MN axons should be seen as fine, uniform, smooth, straight processes (Fig. 9F, hatched black arrow). Degenerating axons were seen in the ventral root exit zones in the ventral funiculus (Fig. 9F). Axonal degeneration was inconspicuous in age-matched controls (Fig. 9D).

Immunostaining patterns for GFAP in the spinal cord were used as an indication of astroglial reactive changes that coincide with neurodegeneration. In age-matched non-tg control spinal cord, the GFAP immunoreactivity was low,

protein NeuN (brown cells). Sections were counterstained with CV. NeuN is present in the nucleus and cytoplasm of mouse MNs (inset) Scale bar (E and F): 32 μm; inset: 15 μm. (**F**) NeuN-positive α-MNs were depleted in ventral horn of hSOD1^{mus} tg mice (line 25 is shown). Attritional α-MNs in mutant hSOD1^{mus} tg mice (line 25 is shown) have apoptotic changes such as fragmentation of the NeuN-positive nucleus into smaller round masses (inset, arrow). Scale bar inset: 15 μm. Sections were counterstained with CV. (**G**) Graph of lumbar NeuN-positive α-MN numbers in control non-tg mice and hSOD1^{mus} tg mice expressing wild-type and mutant hSOD1 (different lines for each construct are grouped). Values are mean ± SEM. G37R, G93A and wild-type hSOD1^{mus} tg mice have a significant loss (*P* < 0.05) of α-MNs. (**H**) Western blot for the MN neurotransmitter-synthesizing enzyme ChAT in soluble protein extracts of total spinal cord from age-matched (12–15 months) non-tg mice and hSOD1^{mus} tg mice expressing G93A variant (lines 112 and 98). Equivalent protein loading is shown by the Ponceau S-stained membrane.
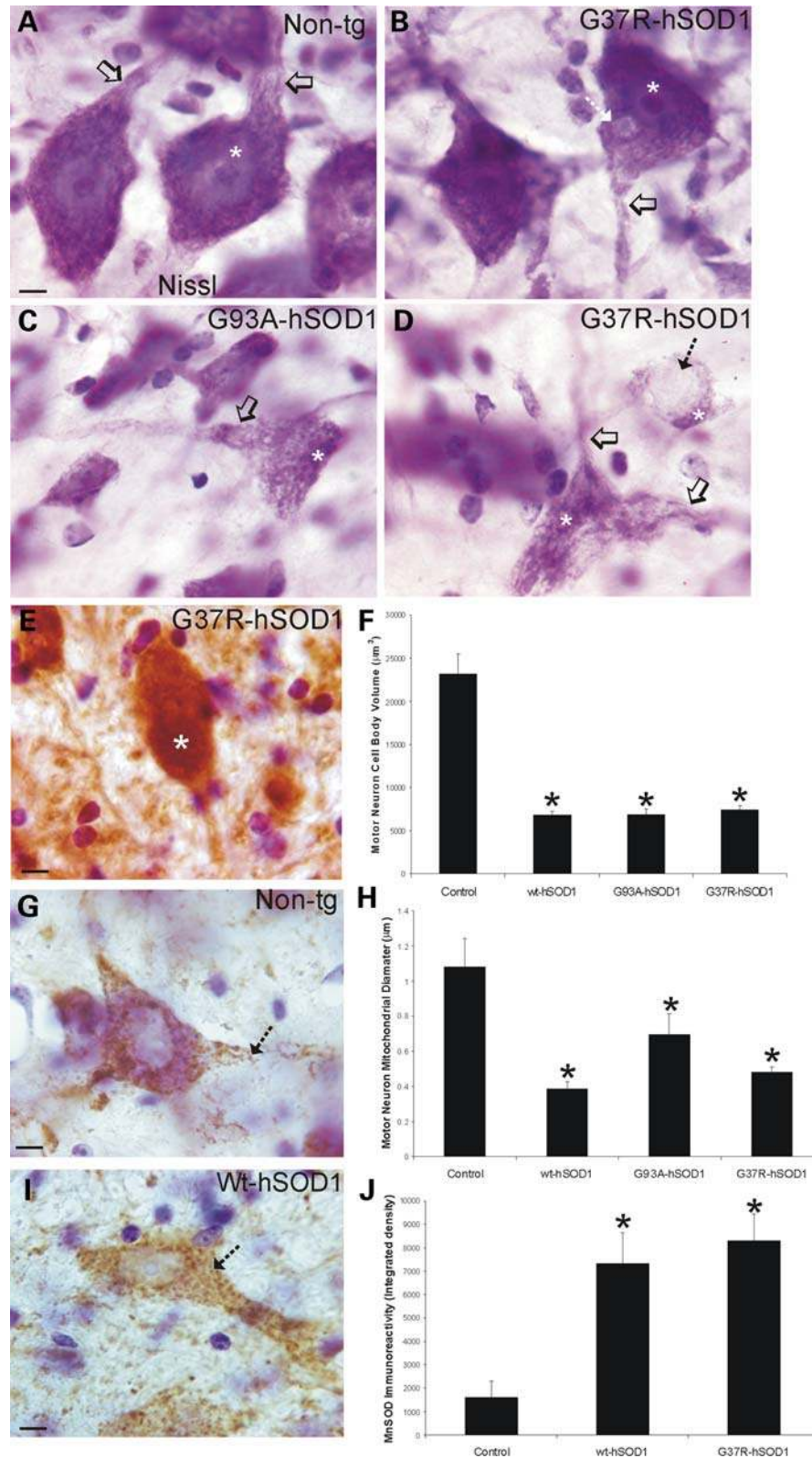
Figure 8. Characteristics of the spinal MN degeneration in hSOD1^{mus} tg mice. (**A–D**) Appearance of MNs in Nissl-stained sections of spinal cord from non-tg (A) and hSOD1^{mus} tg mice expressing G37R (B and D) or G93A (C) mutations at 10–15 months of age. Control MNs have large cell bodies rich in Nissl substance and broad proximal dendrites extending from the perikaryon (A, open arrow). The nucleus (A, asterisk) is open and large with a prominent nucleolus. Scale bar (A–D): 8 μm. (B) In G37R mutants (line 59 is shown), early features of MN degeneration were dendrite attrition (open arrow) and inclusion formation in the cytoplasm of MN cell bodies (hatched arrow). (C and D) Later stage degeneration of MNs in G93A (C) and G37R (D) mutants, lines 112 and 73 are shown respectively, was characterized by: (i) loss of Nissl substance; (ii) formation of vacuoles in the cell body and proximal dendrites with shrinkage (open arrows) and

and GFAP-positive astrocytes were small and not reactive (Fig. 9G, arrows). In contrast, GFAP staining in mutant hSOD1[mus] tg mouse spinal cord was robust, and individual astroglial cells were reactive (Fig. 9H, arrows), particularly in the locations of MNs and where their axons travel in the ventral funiculus (Fig. 9H, arrows).

Experiments were performed to examine potential cell death mechanisms of MNs in hSOD1[mus] tg mice. Silver staining was used to identify degenerating MNs. In non-tg control spinal cord, all MNs were free of silver staining except for the dark nucleolus (Fig. 10A, open arrow). MNs in mutant hSOD1[mus] tg mice showed silver staining patterns indicative of apoptosis (Fig. 10B). Subsets of MNs in silver-stained spinal cord sections of mutant hSOD1[mus] tg mice were shrunken, rounded-up with narrow atrophic proximal dendrites and had a collapsed silver-positive (argyrophilic) nucleus (Fig. 10B, open arrow). Mice were then evaluated for cell death molecule activation in MNs. Spinal cord sections were immunolabeled for cleaved caspase-3. Most MNs in age-matched (10–15 months old) non-tg littermate controls were negative for cleaved caspase-3 (Fig. 10C), and careful cell counting throughout the lumbar spinal cord ventral horn revealed very few MNs positive for cleaved capsase-3 in controls (Fig. 10E). In mutant hSOD1[mus] tg mice, ∼50% of MNs were immunopositive for cleaved caspase-3 (Fig. 10D and E). We used western blotting for caspase-3 in spinal cord extracts to confirm the immunohistochemical evidence for apoptosis in hSOD1[mus] tg mice. Cleaved capsase-3 was detected in mutant hSOD1[mus] tg mouse spinal cord but not in age-matched non-tg spinal cord (Fig. 10F). There was a prominent reduction in full-length pro-enzyme in mutant hSOD1[mus] tg mice compared with age-matched non-tg controls (Fig. 10F).

DISCUSSION

Our major finding is that skeletal muscle expression of hSOD1 is sufficient to cause MN disease in mice. Thus, disease in skeletal muscle is an initiating causal pathologic process in ALS and is not merely secondary neurogenic atrophy. hSOD1 gain of function is directly toxic to skeletal muscle cells and causes their death *in vivo*. This toxicity to skeletal muscle cells involves oxidative damage and nitrative stress, but appears to be independent of the formation of SOD1 aggregates. NMJ abnormalities, distal axonopathy, target deprivation and apoptosis all appear to contribute to the mechanisms of MN loss in the spinal cord of hSOD1[mus] tg

mice, thus demonstrating, for the first time, that skeletal muscle disease or injury can trigger MN degeneration as a mechanism for ALS.

This study reports on the creation and characterization of a new tg mouse model of MN disease caused by hSOD1 expression in skeletal muscle. The muscle-specific expression of hSOD1 was unequivocal; expression of hSOD1 was not found in any tissues studied other than skeletal muscle. Importantly, there was no expression of hSOD1 detected in the brain or spinal cord. The expression of hSOD1 in our mice was low, but levels are comparable with the low-expressing G93A-mSOD1 tg mice that also present with a delayed (∼8 months) disease onset (45). One other published study has shown that muscle-specific expression of G93A-mSOD1 in tg mice causes skeletal muscle toxicity as seen by functional data, histological evidence and biochemical measurements of protein oxidative damage (46). They also reported, as we do, evidence for glial reactive changes in the spinal cord (46), but a fundamental distinction between our study and this earlier study is that we found significant MN degeneration in our mice, whereas Dobrowolny *et al*. (46) did not. The most likely reason for this difference is that we allowed our mice to become old, whereas Dobrowolny *et al*. (46) did their analyses on young 1–4-month-old mice. Nevertheless, both studies show that skeletal muscle is a primary target of hSOD1 toxicity in mice.

We found that mice expressing mutant hSOD1 variants (G93A or G37R) and those expressing wild-type hSOD1 developed disease. Similar phenotypes were observed in motor function tests, skeletal muscle biochemical abnormalities and magnitude of MN loss. Mutant hSOD1[mus] tg mice appeared to develop more MN degeneration compared with wild-type hSOD1[mus] tg mice when Nissl-stained ventral horn MNs were counted (Fig. 7D), but when α-MNs were counted, as identified specifically by NeuN expression (40), wild-type and mutant hSOD1[mus] tg mice showed similar losses (Fig. 7G). The wild-type construct was intended as a control, but multiple lines of wild-type hSOD1[mus] tg mice developed muscle pathology. Although this result was surprising, the literature reveals precedent for overexpression of wild-type hSOD1 causing harmful effects and disease in mouse models and in cell culture. Tg mice expressing wild-type hSOD1 develop premature aging abnormalities at the NMJ (47,48) and muscular dystrophy (49). Sciatic nerve regeneration is impaired in mice overexpressing wild-type hSOD1 (50), and excitotoxicity is exacerbated in the brain and in cultured neurons in the presence of wild-type

(iii) displacement and condensation of the nucleus (asterisk). Some MNs were found with large cytoplasmic inclusions (D, hatched arrow). (**E**) Some MNs had large cytoplasmic inclusions that were positive for ubiquitin (white asterisk). Sections were counterstained with CV. Scale bar (inset): 8 μm. (**F**) Graph of lumbar MN cell body volumes in control non-tg mice and hSOD1[mus] tg mice expressing wild-type and mutant hSOD1 (different lines for each construct are grouped). Values are mean ± SEM. G37R, G93A and wild-type mice have a significant MN cell body attrition (asterisks, $P < 0.05$). (**G**) Immunohistochemistry for the mitochondrial marker MnSOD shows that large multipolar MNs in the ventral horn of non-tg mice have many divisible particles of immunoreactivity (hatched arrow) representing individual mitochondria distributed within their perikaryon and proximal dendrites. Sections were counterstained with CV. Scale bar: 10 μm. (**H**) Graph of mitochondrial diameters in lumbar MN cell bodies and proximal dendrites in control non-tg mice and hSOD1[mus] tg mice expressing wild-type and mutant hSOD1 (different lines for each construct are grouped). Values are mean ± SEM. G37R, G93A and wild-type mice have significantly (asterisks, $P < 0.05$) smaller mitochondria in remaining or attritional MNs. (**I**) Representative lumbar spinal MN from a wild-type-hSOD1[mus] tg mouse (line 224) showing the accumulation of small mitochondria (hatched arrow) within the cell body and proximal dendrite. Sections were counterstained with CV. Scale bar: 10 μm. (**J**) Graph of total MnSOD immunoreactivity, determined by single-cell densitometry, in lumbar MN cell bodies and proximal dendrites in control non-tg mice and hSOD1[mus] tg mice expressing wild-type- and G37R-hSOD1 (different lines for each construct are grouped). Values are mean ± SEM. G37R and wild-type mice have significantly (asterisks, $P < 0.05$) increased MnSOD immunoreactivity in remaining or attritional MNs.
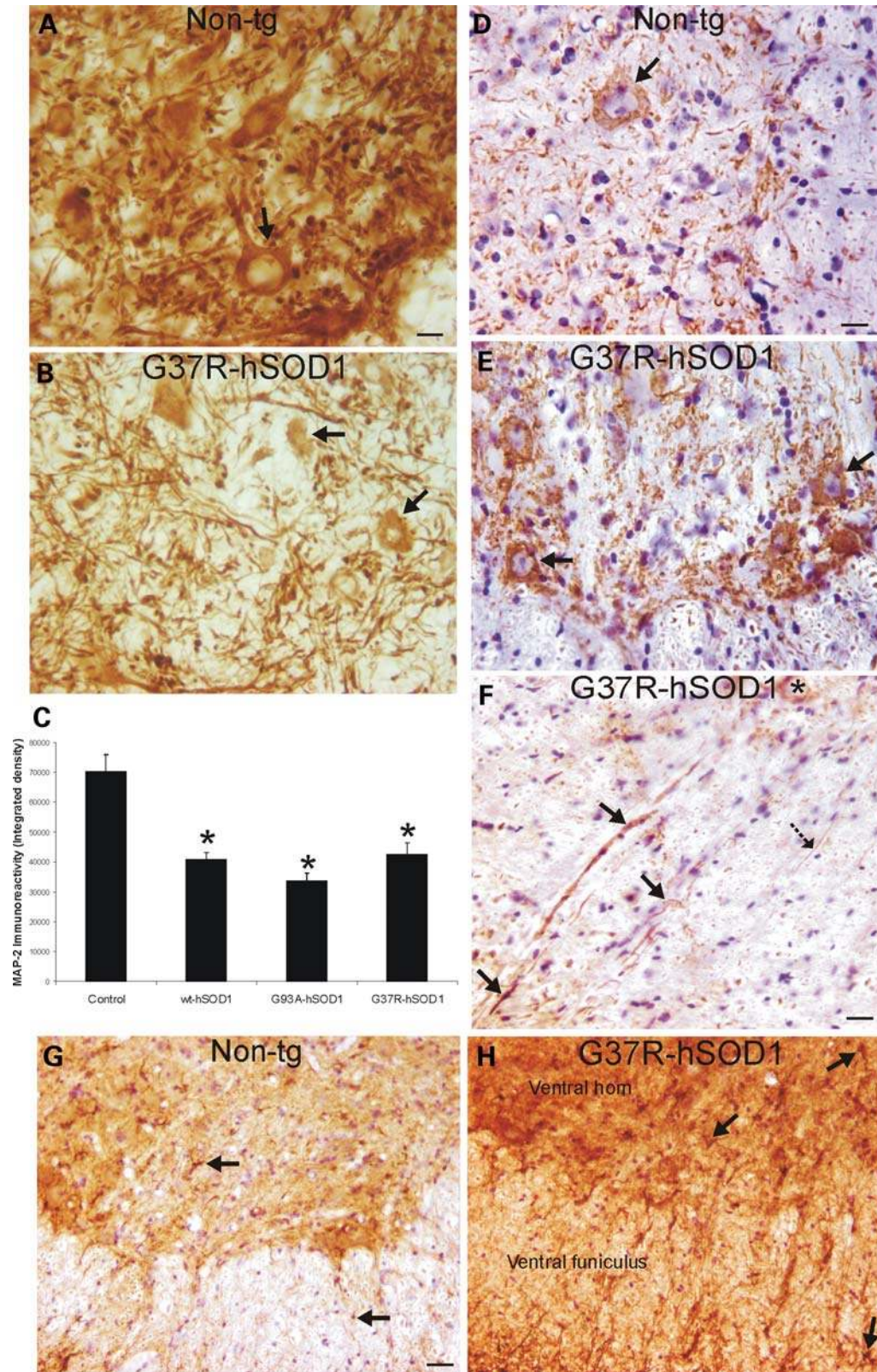
Figure 9. hSOD1[mus] tg mice have cytoskeletal abnormalities consistent with spinal MN degeneration. (**A** and **B**) Immunohistochemistry shows that the soma-todendritic cytoskeletal protein MAP2 is enriched (brown staining) in individual spinal MNs (A, arrow) and is very concentrated in the neuropil of non-tg mice, whereas it is depleted in the ventral horn of hSOD1[mus] tg mice (line 85), and individual MAP2-positive MNs are attritional and without major proximal dendrites (B, arrows). Scale bar (A and B): 26 μm. (**C**) Graph of total MAP2 immunoreactivity, determined by densitometry, in lumbar spinal cord ventral horn in age-matched control non-tg mice and hSOD1[mus] tg mice expressing wild-type and mutant hSOD1 (different lines for each construct are grouped). Values

hSOD1 (51). In cell culture, oxidized wild-type hSOD1 can cause dose-dependent cell death like mutant hSOD1 variants (11). Moreover, zinc deficiency can render wild-type SOD1 toxic to MNs in culture through mechanisms involving a gain in redox reactivity and catalysis of tyrosine nitration in proteins (52). Our tg mice expressing wild-type and mutant hSOD1 show evidence for oxidative stress and severe protein nitration in skeletal muscle consistent with the possibility that wild-type hSOD1 might acquire toxic properties through redox chemistry, thereby contributing to skeletal muscle damage.

We show that hSOD1^{mus} tg mice develop robust neurologic and histopathologic phenotypes consistent with MN disease. hSOD1^{mus} tg mice show progressive, age-related loss of activity, weakness and paresis. The deterioration in motor function seen in hSOD1^{mus} tg mice was paralleled by direct histological evidence for skeletal muscle damage and myofiber loss. The histology of affected skeletal muscle gave a picture of myofiber sarcolysis and cellular necrosis, but western blotting also indicated activation of caspase-3. Plausible explanations for this toxicity to skeletal muscle cells are perturbations in mitochondrial oxidative phosphorylation and altered oxidative chemistry. Enzyme histochemistry and western blots for complex IV in skeletal muscle of hSOD1^{mus} tg mice indicated prominent upregulation, with the latter assay also revealing aggregation of Cox-I. Oxyblot analyses showed elevated levels of protein carbonyls in mitochondria-enriched fractions of hSOD1^{mus} tg mice. Western blotting for 3-nitrotyrosine revealed accumulation of nitrated proteins in skeletal muscle of hSOD1^{mus} tg mice. Previous studies on the G93A-mSOD1 (original H1 line, non-tissue specific, ubiquitously expressed at high levels) tg mouse have shown evidence for oxidative damage in skeletal muscle (36) as well as profound metabolic and contractile perturbations (34,35). Skeletal muscle in these mice is hypermetabolic (35), has mitochondrial defects in intracellular Ca^{2+} signaling (53) and has a 12-fold higher generation of mitochondrial reactive oxygen species (54). In our tg mice, hSOD1 was detected in soluble and mitochondria-enriched fractions of skeletal muscle. The association of hSOD1 with skeletal muscle cell mitochondria and evidence of oxidative/nitrative damage converge on the idea that hSOD1 gains dominant toxic redox reactive properties within skeletal muscle to alter mitochondrial function in hSOD1^{mus} tg mice.

We observed that restricted expression of hSOD1 in mouse skeletal muscle causes dismantled NMJs and MN distal axonopathy. Symptomatic hSOD1^{mus} tg mice had a greater frequency of unoccupied motor endplates compared with age-matched non-tg control mice. Similar abnormalities occur in the G93A-mSOD1 tg mouse (39,55,56). The possibility that MN distal axonopathy is an early initiating mechanism of ALS has been proposed before, but not tested (55). One study has shown elegantly that G93A-mSOD1 tg mice with muscle-restricted expression of local IGF1 have protected NMJs, enhanced MN survival, delayed disease onset and extended lifespan (57). However, use of an siRNA and deletable mutant hSOD1 gene to diminish mutant protein in skeletal muscle failed to affect disease in mice (58), but the downregulation involved limited muscle groups and was very incomplete and likely to be insufficient to alter disease progression at a whole-animal level. In a different tg model, mice with restricted overexpression of mitochondrial uncoupling protein-1 in skeletal muscle developed age-related deterioration of the NMJ, peripheral nerve axonopathy and MN loss (59). These reports lead us to suspect a link between the skeletal muscle apparent hyper-metabolism and oxidative damage in our mouse model and to tentatively interpret the MN distal axonopathy and denervation of skeletal muscle as a result of toxic actions of hSOD1 in myofibers and NMJ damage. MN pre-synaptic terminals at the NMJ or axonal abnormalities, involving Schwann cell-inducible nitric oxide synthase (60), might trigger a form of retrograde axonal dying-back (53) and degeneration of MNs.

We discovered that restricted expression of hSOD1 in skeletal muscle of tg mice was sufficient to cause MN degeneration and loss. This degeneration of MNs had features of somatodendritic attrition, nuclear condensation and capsase-3 activation similar to that seen in human ALS (61,62). Intracellular inclusions were also present in MNs, but they have not yet been immunophenotyped. It is also not yet clear how the toxic process initiated in the skeletal muscle is mediated from the NMJ. This could involve MN neurotrophin deprivation of skeletal muscle or axon-derived factors (63) or retrograde transport of synapse-derived mitochondria with altered redox states serving as toxic harbingers from distal sites (43). In any event, it is noteworthy that the morphology of the MN degeneration in hSOD1^{mus} tg mice is the closest to that occurring in human ALS which we have seen so far in multiple mouse models of ALS (43,64–66).

hSOD1^{mus} tg mice could be a physiologically more relevant model of ALS than other hSOD1 tg models reported to date because of their slow clinical course and age-related pathology. The prolonged disease course in our mice could be related to the level of expression of hSOD1 in skeletal muscle which might be insufficient to cause rapid onset disease. Another possibility is that the enodogenous regenerative capacity of skeletal muscle (67) is sufficient to prolong the disease course in our mice and thus makes aging a

---

are mean ± SEM. Tg mice have significantly (asterisks, $P < 0.05$) decreased MAP2 immunoreactivity in ventral horn. (**D** and **E**) In spinal cord sections stained immunohistochemically for phosphorylated neurofilament (using immunoperoxidase with DAB, brown staining), there was only faint labeling in the MN cell bodies in controls (D), whereas age-matched mutant-hSOD1^{mus} tg mice (line 85) showed prominent accumulation of phosphorylated neurofilament in cell body of MNs (E, arrows). Sections were counterstained with CV. Scale bar (D and E): 26 μm. (**F**) Within white matter near the ventral root exit zone of mutant-hSOD1^{mus} tg mice (line 25), subsets of axons positive for phosphorylated neurofilament (brown staining) were dystrophic, appearing as swollen or tortuous (arrows), whereas other axons appeared normal as uniform, fine filaments (hatched solid black arrow). A ventral horn MN has accumulated phosphorylated neurofilament in the cell body (asterisk). Section was counterstained with CV. Scale bar: 24 μm. (**G** and **H**) In lumbar spinal cord sections stained immunohistochemically for GFAP (using immunoperoxidase with DAB, brown staining), controls had low immunoreactivity, and individual astrocytes in gray matter and white matter were small and non-reactive (G, arrows); in contrast, mutant-hSOD1^{mus} tg mice (line 73) showed dark immunoreactivity (H), compared with age-matched control (G), indicative of reactive astrogliosis. Individual astrocytes in mutant-hSOD1^{mus} tg mouse spinal cord were large and reactive (H, arrows). Sections were counterstained with CV. Scale bar (G and H): 68 μm.
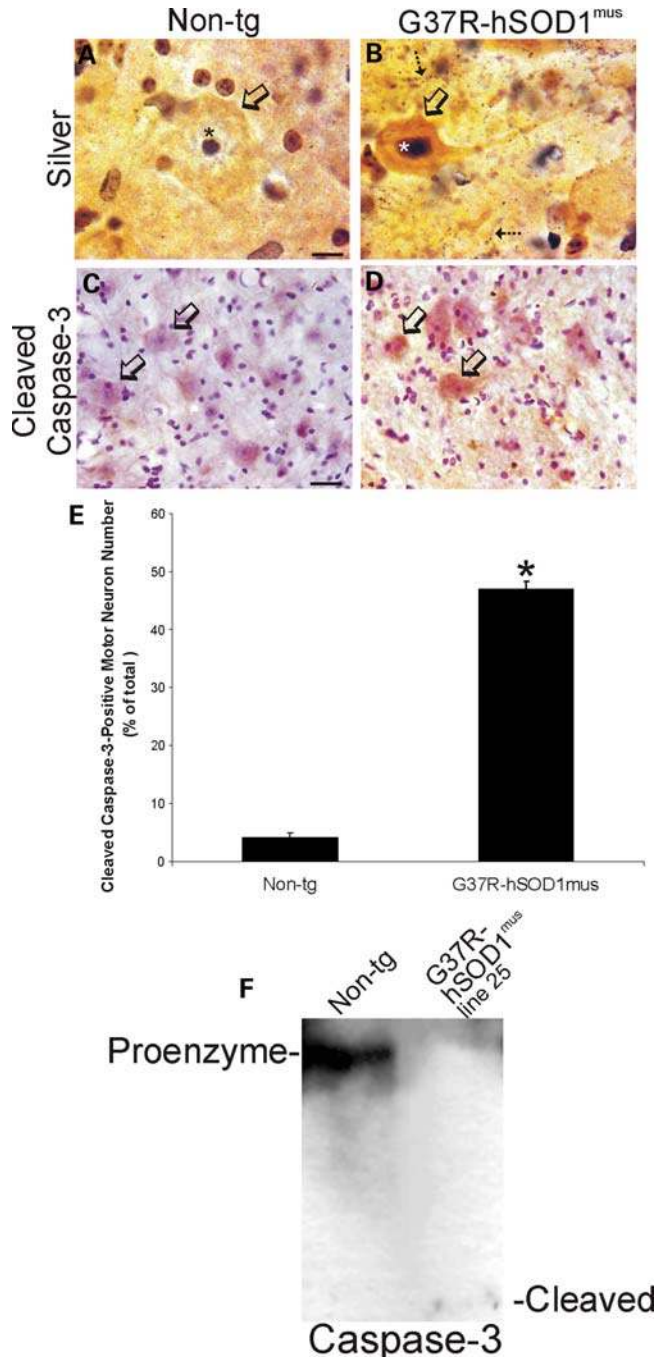
Figure 10. Degeneration of spinal MNs in hSOD1^{mus} tg mice is apoptotic-like. (**A** and **B**) Silver staining in control mouse spinal cord showed that MN cell bodies (A, open arrow), their nuclei (A, asterisk) and the surrounding neuropil were free of degeneration, whereas mutant-hSOD1^{mus} tg mouse (line 73) MNs showed somatodendritic attrition with nuclear condensation (B, open arrow), and the neuropil contained numerous degenerating processes (B, hatched arrows). Scale bar (A and B): 8 μm. (**C** and **D**) In spinal cord sections stained immunohistochemically for cleaved capsase-3 (using immunoperoxidase with DAB, brown staining), faint granule-like labeling was observed in the cytoplasm of few MN cell bodies in 12–15-month-old controls (C), whereas age-matched mutant-hSOD1^{mus} tg mice (line 73) showed accumulation of cleaved caspase-3 in the cell body of subsets of MNs (D, open arrows). Sections were counterstained with CV. Scale bar (C and D): 28 μm. (**E**) Graph of the number of lumbar MNs that were positive for cleaved caspase-3 in control non-tg mice and hSOD1^{mus} tg mice expressing

greater risk factor for disease onset. This effect in our mice would be relevant physiologically to human ALS considering the average age of onset of human ALS patients is ~55 years. Our new tg mouse might also be able to shed light on how wild-type SOD1 can be toxic in non-familial ALS, which represent the vast majority of ALS patients. In light of our findings, the skeletal muscle changes in human ALS need to be examined more closely and re-evaluated for molecular mechanism-based therapies targeting skeletal muscle.

MATERIALS AND METHODS

Design of hSOD1^{mus} gene constructs and generation of tg mice

The construct design used for the creation of hSOD1^{mus} tg mice is shown in Figure 1A. A 247 bp *ClaI/XmaI* fragment containing the chicken skeletal muscle α_{sk} actin promoter from the plasmid CLA12-191αACTCAT1 (68) was cloned into the *ClaI/XmaI* multiple cloning site of the pBluescript IISK(+) phagemid (Stratagene). This promoter has been used to create several lines of tg mice with muscle-specific expression of exogenous proteins (68). The G37R and G93A mutations were introduced into the hSOD1-coding sequence of the entry clone IOH4089 (Invitrogen) using the Quik-Change II Site-Directed Mutagenesis kit (Stratagene). Wild-type and mutant hSOD1 cDNA sequences were amplified by PCR from the entry clones using 5′ and 3′ primers flanked by *Bam*HI restriction sites. The 3′ primer also contained ATTAAA, the polyadenylation signal 5′ to the *Bam*HI site. The 555 bp amplified product was cloned into the *Bam*HI cloning site in pBluescript, 3′ to the chicken α_{sk} actin promoter. All sequences were confirmed by sequencing in both forward and reverse directions. To create tg mice, the three plasmids were digested with *Apa*LI, resulting in a 2.5 kb fragment. The fragments were given to the Johns Hopkins Transgenic Core Facility for injection into B6SJLF1 mouse embryos. The Institutional Animal Care and Use Committee approved the animal protocols.

Tg positives were confirmed by PCR analysis of tail genomic DNA using three different primer pairs. Mouse tails were digested using DirectPCR Lysis Reagent (Viagen Biotech), and DNA was extracted from the lysate by precipitation with isopropanol. The presence of the transgene was confirmed by PCR with the following sets of primers: 5′-GCCCGCCTCGA TAAAAGGCT-3′ and 5′-GCGCGCAATTAACCCTCACT-3′ (719 bp), 5′-GCAGAAGGAAAGTAATGGAC-3′ and 5′-GAA AGCTGGGTTCTATTGGG-3′ (412 bp), 5′- GCAGAAGGAA AGTAATGGAC-3′ and 5′-GTACAGCCTGCTGTATTATC-3′ (111 bp).

mutant hSOD1. Values are mean ± SEM (different lines for each construct are grouped). Mutant-hSOD1^{mus} tg mice had a significant increase ($P <$ 0.01) in the number of cleaved caspase-3$^+$ MNs. (**F**) Western blot for caspase-3 in soluble protein extracts of total spinal cord of a mutant-hSOD1^{mus} tg mouse (line 25 is shown) and an age-matched non-tg mouse. In non-tg mouse spinal cord, full-length 32 kDa pro-enzyme is detected strongly, but no cleaved (12 kDa) subunit is detected. In contrast, in G37R-hSOD1^{mus} tg mouse spinal cord, the pro-enzyme level is reduced markedly and cleaved subunit is detected.

PCR was performed using a Techne thermocycler with a 2 min preheating at 95°C, followed by 35 cycles of denaturation at 95°C, 1 min, annealing at 55°C, 1 min and extension at 72°C, 1 min. Amplification was completed with an additional 7 min extension at 72°C. All PCR products contained coding region of hSOD1 gene.

For Southern analysis, DNA was extracted from mouse tails by phenol/chloroform extraction. The probe (Fig. 1A) was a *Sac*II-digested fragment of the construct spanning the entire chicken α_{sk} actin promoter and the coding region of hSOD1. Prior to electrophoresis, genomic DNA was digested with *Nco*I, which has a single restriction cleavage site within the hSOD1-coding region in the transgene construct. For control samples, digested tail DNA from non-tg mice was spiked with various amounts of *Apa*LI-digested construct and electrophoresed alongside tg samples. Southern analysis was performed using the DIG High Prime DNA Labeling and Detection Starter Kit II (Roche).

For real-time qPCR, the set of genotyping primers which gave a 412 bp product was used. Briefly, genomic DNA was extracted from mouse tails using the GenElute™ Mammalian Genomic DNA Miniprep Kit (Sigma-Aldrich). Tail DNA (50 ng) was added to a reaction mixture consisting of 2x iQ SYBR Green Supermix, 50 nM each of forward and reverse primers in a total volume of 25 μl. Each sample was amplified in triplicate. After an initial enzyme activation of 5 min at 95°C, 30 cycles of 95°C for 30 s and 60°C for 1 min were performed and results were analyzed using the Bio-Rad iQ™5 Real–Time PCR Detection System. As standards, 10^3–10^7 copies of transgene plasmid vector were used.

Assessment of neurologic deficits in hSOD1[mus] tg mice

tg hSOD1[mus] mice and age-matched non-tg littermate controls were studied longitudinally every week beginning at 1 month of age for neurologic deficits. They were assessed beginning at 6 months of age using a wire hang-time test and a voluntary activity wheel (Harvard Apparatus).

Immunoblotting

Western blot analysis was performed to examine expression of hSOD1, Cox-I, nitrated proteins and caspase-3 in skeletal muscle, brain or spinal cord. hSOD1[mus] tg mice at 2–4 months of age ($n = 4$–6/genotype) and 10–12 months of age ($n = 4$–6/genotype) as well as age-matched non-tg littermate control mice ($n = 4$–6/genotype/age) were deeply anesthetized with a lethal dose of chloral hydrate and decapitated for harvesting forelimb (triceps) and hind-limb (gluteus, biceps and gastrocnemius pooled) skeletal muscle, brain and spinal cord, which were quickly frozen on dry ice. These samples were minced or pulverized and homogenized with a Brinkmann polytron in ice-cold 20 mM Tris–HCl (pH 7.4) containing 10% (wt/vol) sucrose, 200 mM mannitol, Complete protease inhibitor cocktail (Roche), 0.1 mM phenylmethylsulfonyl fluoride, 10 mM benzamidine, 1 mM EDTA and 5 mM EGTA. Crude homogenates were sonicated for 15 s and then centrifuged at $1000g_{av}$ for 10 min (4°C). The supernatant was centrifuged at $54\,000g_{av}$ for 20 min (4°C) to yield soluble (S2) and mitochondria-enriched pellet (P2) fractions.

This subcellular fractionation protocol has been verified (69). The pellet fraction was washed (twice) by trituration in homogenization buffer followed by centrifugation and then finally resuspended in homogenization buffer (without sucrose) supplemented with 20% (wt/vol) glycerol. Protein concentrations were measured by a Bio-Rad protein assay with bovine serum albumin as a standard.

Proteins from skeletal muscle and spinal cord were subjected to sodium dodecyl sulfate–polyacrylamide gel electrophoresis (SDS–PAGE) and transferred to nitrocellulose membrane by electroelution as described (69). The reliability of sample loading and electroblotting in each experiment was evaluated by staining nitrocellulose membranes with Ponceau S before immunoblotting. Ponceau S-stained membranes were scanned for documentation of protein loading and even transfer among lanes. If transfer was not uniform, blots were discarded and gels were run again. Blots were blocked with 2.5% non-fat dry milk with 0.1% Tween 20 in 50 mM Tris-buffered saline (pH 7.4), then incubated overnight at 4°C with a rabbit polyclonal antibody to SOD1 (Assay Designs), mouse monoclonal antibody to Cox-I (Invitrogen, Molecular Probes), mouse monoclonal antibody to MyoD (BD Bioscience), rabbit polyclonal antibodies to caspase-3 (Santa Cruz Biotechnology), rabbit monoclonal antibody to synaptophysin (Abcam) and goat polyclonal antibody to ChAT (Chemicon). The antibodies were used at concentrations for visualizing protein immunoreactivity within the linear range. As a protein-loading control, some blots were re-probed with monoclonal antibody to glyceraldehyde phosphate dehydrogease (GAPDH). After the primary antibody incubation, blots were washed and incubated with horseradish peroxidase (HRP)-conjugated secondary antibody (0.2 μg/ml), developed with enhanced chemiluminescence (ECL, Pierce) and exposed to X-ray film.

Histology and immunohistochemistry

Mutant and wild-type hSOD1[mus] tg mice at pre-symptomatic ($n = 6$–8/genotype) and symptomatic stages ($n = 6$–10/genotype) of disease and age-matched non-tg littermate control mice ($n = 6$–10) were deeply anesthetized and perfusion-fixed using 4% paraformaldehyde (PF). After perfusion-fixation, forelimb triceps muscle, hind-limb gluteus, biceps femoris, gastrocnemius muscles and spinal cord were removed from each mouse, and the tissues were cryoprotected (20% glycerol) before they were frozen-sectioned (40 or 80 μm) using a sliding microtome. Serial section arrays were stored individually in 96-well plates. Skeletal muscle samples from non-tg and tg mice were also prepared using paraffin processing and sectioning at 10 μm. Skeletal muscle samples were cut in transverse and longitudinal planes, whereas spinal cord was cut only in the transverse plane.

Skeletal muscle was examined for pathology in transverse and longitudinal planes by H&E staining, TUNEL and enzyme histochemistry. Paraffin and frozen sections were used for H&E staining. Paraffin sections were used for TUNEL as described (70) and counterstained with eosin. ATPase activity (pH 9.4) was visualized in sections of gastrocnemius and quadriceps using a histochemical protocol (71)

with modifications (43). Cox enzyme histochemistry was done as before (43).

The spinal cord was examined for pathology using Nissl staining using cresyl violet (CV), silver staining and immunohistochemistry. CV staining was done on every 10th section of lumbar and cervical spinal cord. Silver staining was used to visualize degenerating neuronal elements in every 11th spinal cord section using the FD NeuroSilver kit (FD Neurotechnologies, Inc., Baltimore, MD, USA). The localization patterns of hSOD1, NeuN, MnSOD, MAP2, phosphorylated neurofilament, ubiquitin, GFAP and cleaved caspase-3 were examined at the light microscopic level using an immunoperoxidase method with diaminobenzidine (DAB) as chromogen. Human-specific SOD1 was detected with a mouse monoclonal antibody (Clone 1G2, MBL, International, Woburn, MA, USA) diluted at 1:1000. NeuN was detected with a monoclonal antibody (MAB377, Chemicon) diluted at 1:500. MnSOD was detected with two different rabbit polyclonal antibodies (SOD-110 and SOD-111, Stressgen) diluted at 1:500. MAP2 was detected with a monoclonal antibody (clone AP2, Boehringer Mannheim, Indianapolis, IN, USA). Phosphorylated neurofilament was detected with mouse monoclonal antibody SMI-31 (Covance) diluted at 1:10 000. Ubiquitin was detected with a rabbit polyclonal antibody (Sigma) diluted at 1:1000. GFAP was localized using a rabbit polyclonal antibody diluted at 1:5000. Cleaved caspase-3 was detected with a rabbit polyclonal antibody (1:1000) to the active subunits (Cell Signaling).

Cell counting

Skeletal muscle and spinal cord of tg and non-tg mice were evaluated for loss of cells. Systematically random sampled transverse paraffin sections stained with H&E were used to estimate the numbers of gastrocnemius myofibers by profile-counting at $1000\times$ (at least three different sections per mouse muscle as counted). Nissl-stained transverse sections of spinal cord were used to count the number of MNs. For Nissl-staining, spinal cord sections were selected with a random start and then systematically sampled (every 10th section) to generate a subsample of sections from each mouse lumbar and cervical spinal cord that were mounted on glass slides for staining with CV for evaluation. Nissl-stained MNs were counted at $\times 400$ magnification using strict morphologic criteria. These criteria included a round, open, pale nucleus (not condensed and darkly stained), globular Nissl-staining of the cytoplasm and a diameter of $\sim 25-40\ \mu m$. With these criteria, astrocytes, oligodendrocytes and microglia were excluded from the counts, but these counts are likely to estimate the combined populations of α-MNs and γ-MNs. We therefore used expression of NeuN to distinguish α-MNs from γ-MNs (40). Spinal cord sections were selected with a random start and then systematically sampled to generate a subsample of sections from each mouse lumbar spinal cord to stain immunocytochemically for NeuN and afterwards mounted on glass slides and counterstained with CV for counting. Morphologically intact NeuN$^+$ α-MNs with a visible nucleus were counted in each hemisection of lumbar spinal cord from tg and non-tg mice. A similar

strategy was used for the determination of cleaved caspase-3$^+$ MNs in immunolabeled lumbar spinal cord sections.

Single-cell measurements and ocular filar micrometry

Nissl-stained sections of lumbar spinal cord were used to determine MN cell body volume. MNs were observed at $\times 1000$ magnification, and with a calibrated ocular micrometer, the major axis diameter (including the largest proximal dendrite) and the minor axis diameter was measured for 25–50 different MNs in each mouse. Cell body volume was calculated from the equation $V = (\pi/6)ab^2$, where a is the diameter of major axis and b is the diameter of minor axis (72). Lumbar spinal cord sections stained with antibodies to MnSOD were used to determine mitochondrial diameters within the cell body of individual MNs (43) in tg and non-tg mice, using ocular filar micrometry. To estimate individual MN mitochondrial content, lumbar spinal cord sections stained with antibodies to MnSOD were analyzed quantitatively with single-cell densitometry (64,73) using ImageJ software. For each mouse, approximately 25 MN neuron profiles, cut through the approximate cell center as judged by the nucleus, were delineated as the region of interest. Relative immunoreactivity level is reflected by the average-integrated optical density immunoreaction product.

NMJ analysis

To study the NMJ in hSOD1^{mus} tg mice, motor endplates were visualized using fluorescent-conjugated BTX, which binds irreversibly to post-synaptic acetylcholine receptors on the skeletal muscle plasma membrane (74). After perfusion with PF, the gluteus, biceps femoris and medial gastrocnemius muscles were dissected carefully, cryoprotected overnight in 20% glycerol and sectioned at 40 μm on a freezing microtome. Each muscle was sectioned completely so that all NMJs could be evaluated. Motor endplates were visualized with Alexa 594-conjugated BTX (Invitrogen) as described (22). Dual-labeling was done to visualize MN distal axons and their terminals in skeletal muscle by immunofluorescent detection of either neurofilament protein using a monoclonal antibody (SMI-32, Convance) or synaptophysin using a polyclonal antibody (Dako). Sections were viewed and analyzed using a Zeiss Axiphot epifluorescence microscope. The immunofluorescent labeling for neurofilament and synaptophysin was used to determine whether the endplates were innervated. In randomly selected digital images, endplates were scored as innervated (normal) if there was complete overlap with the axon terminal or denervated (unoccupied) if the endplate was not associated with an axon. Some endplates were associated with an apparent preterminal axon only or showed only partial overlap. These were not included in this data set.

Protein oxidation and protein nitration

To detect oxidative modification of proteins in mSOD1 mouse spinal cord, we used an OxyBlot protein oxidation detection kit (Chemicon) for carbonyl groups. Aliquots of equal amounts of protein (10 μg) were denatured with 10% SDS, then derivatized to 2-4-dinitrophenylhydrazone (DNP)

by a reaction with 2-4-dinitrophenylhydrazine (DNPH) for exactly 5 min. This reaction allows for a chemical conjugation of the DNPH to the carbonyl group of the protein side chain to create a hydrazone moiety that can be immuno-detected. The reaction was quenched with a neutralizing solution (6% SDS), and a characteristic color change to brown followed. Samples were then placed on ice and loaded onto 10% gels for SDS–PAGE. Proteins with conjugated DNP residues were detected with polyclonal rabbit antibody DNP used at a concentration of 1:150. Proteins were then visualized with goat anti-rabbit HRP-conjugated antibody and ECL.

Nitrated proteins were detected by western blotting. Mitochondria-enriched and soluble subcellular fractions of hind-limb skeletal muscle were subjected to SDS–PAGE and transferred to a nitrocellulose blot. After blocking with 0.1% BSA, 0.1% Tween in 1x PBS for 1 h at room temperature, the membrane was incubated at 4°C overnight with a monoclonal antibody specific for 3-nitrotyrosine in nitrated proteins (Millipore, Upstate, NY, USA) in blocking buffer at a dilution of 1:40 000. The membrane was then incubated with an HRP-conjugated anti-mouse secondary antibody (1:10 000) in blocking buffer for 1 h at room temperature. The nitrated proteins were visualized using an ECL detection kit (Pierce) on Kodak X-ray films.

Data analysis

The values shown in the graphs represent the mean $\pm$ standard error of the mean (SEM). Group means and variances were evaluated statistically by one-way ANOVA and a Student's *t*-test.

Photography and figure construction

The original images used for figure construction were generated using digital photography. Digital images were captured as TIFF files using a SPOT digital camera and SPOT Advanced software (Diagnostic Instruments) or a Nikon digital camera (DXM1200) and ACT-1 software. Images were altered slightly for brightness and contrast using ArcSoft PhotoStudio 2000 or Adobe Photoshop software without changing the content and actual result. Figure composition was done using CorelDraw 9 software, with final figures being converted to TIFF files. Files of composite figures were adjusted for brightness and contrast in Adobe Photoshop.

SUPPLEMENTARY MATERIAL

Supplementary Material is available at *HMG* online.

ACKNOWLEDGEMENTS

Conflict of Interest statement. None declared.

FUNDING

REFERENCES

1. Rowland, L.P. and Shneider, N.A. (2001) Amyotrophic lateral sclerosis. *N. Engl. J. Med.*, **344**, 1688–1700.
2. Chou, S.M. (1992) Pathology—light microscopy of amyotrophic lateral sclerosis. In Smith, R.A. (ed.), *Handbook of Amyotrophic Lateral Sclerosis*. Marcel Dekker, Inc., New York, NY, pp. 133–181.
3. Kabashi, E., Valmanis, P.N., Dion, P. and Rouleau, G.A. (2008) TARDBP mutations in individuals with sporadic and familial amyotrophic lateral sclerosis. *Nat. Genet.*, **40**, 572–574.
4. Deng, H-X., Hentati, A., Tainer, J.A., Iqbal, Z., Cayabyab, A., Hung, W-Y., Getzoff, E.D., Hu, P., Herzfeldt, B., Roos, R.P. *et al.* (1993) Amyotrophic lateral sclerosis and structural defects in Cu,Zn superoxide dismutase. *Science*, **261**, 1047–1051.
5. Rosen, D.R., Siddique, T., Patterson, D., Figiewicz, D.A., Sapp, P., Hentati, A., Donalsson, D., Goto, J., O'Regan, J.P., Deng, H.-X. *et al.* (1993) Mutations in Cu/Zn superoxide dismutase gene are associated with familial amyotrophic lateral sclerosis. *Nature*, **362**, 59–62.
6. McCord, J.M. and Fridovich, I. (1969) Superoxide dismutase. *J. Biol. Chem.*, **244**, 6049–6055.
7. Rakhit, R., Crow, J.P., Lepock, .J.R., Kondejewski, L.H., Cashman, N.R. and Chakrabartty, A. (2004) Monomeric Cu,Zn-superoxide dismutase is a common misfolding intermediate in the oxidation models of sporadic and familial amyotrophic sclerosis. *J. Biol. Chem.*, **279**, 15499–15504.
8. Borchelt, D.R., Lee, M.K., Slunt, H.H., Guarnieri, M., Xu, Z.-S., Wong, P.C., Brown, R.H. Jr, Price, D.L., Sisodia, S.S. and Cleveland, D.W. (1994) Superoxide dismutase 1 with mutations linked to familial amyotrophic lateral sclerosis possesses significant activity. *Proc. Natl Acad. Sci. USA*, **91**, 8292–8296.
9. Yim, M.B., Kang, J.-H., Yim, H.-S., Kwak, H.-S., Chock, P.B. and Stadtman, E.R. (1996) A gain-of-function of an amyotrophic lateral sclerosis-associated Cu, Zn-superoxide dismutase mutant: an enhancement of free radical formation due to a decrease in K_m for hydrogen peroxide. *Proc. Natl Acad. Sci. USA*, **93**, 5709–5714.
10. Kabashi, E. and Valdmanis, P.N. (2007) Oxidized/misfolded superoxide dismutase-1: the cause of all amyotrophic lateral sclerosis? *Ann. Neurol.*, **62**, 553–559.
11. Ezzi, S.A., Urushitani, M. and Julien, P. (2007) Wild-type superoxide dismutase acquires binding and toxic properties of ALS-linked mutant forms through oxidation. *J. Neurochem.*, **102**, 170–178.
12. Pramatarova, A., Laganière, J., Roussel, J., Brisebois, K. and Rouleau, G.A. (2001) Neuron-specific expression of mutant superoxide dismutase 1 in transgenic mice does not lead to motor impairment. *J. Neurosci.*, **21**, 3369–3374.
13. Lino, M.M., Schneider, C. and Caroni, P. (2002) Accumulation of SOD1 mutants in postnatal motoneurons does not cause motoneuron pathology or motoneuron disease. *J. Neurosci.*, **22**, 4825–4832.
14. Jaarsma, D., Teuling, E., Haasdijk, E.D., Zeeuw, C.I. and Hoogenraad, C.C. (2008) Neuron-specific expression of mutant superoxide dismutase is sufficient to induce amyotrophic lateral sclerosis in transgenic mice. *J. Neurosci.*, **28**, 2075–2088.
15. Wang, L., Sharma, K., Deng, H.-X., Siddique, T., Grisotti, G., Liu, E. and Roos, R.P. (2008) Restricted expression of mutant SOD1 in spinal motor neurons and interneurons induces motor neuron pathology. *Neurobiol. Dis.*, **29**, 400–408.
16. Gong, Y.H., Parsadanian, A.S., Andreeva, A., Snider, W.D. and Elliott, J.L. (2000) Restricted expression of G86R Cu/Zn superoxide dismutase in astrocytes results in astrocytosis but does not cause motoneuron degeneration. *J. Neurosci.*, **20**, 660–665.
17. Nagai, M., Re, D.B., Nagata, T., Chalazonitis, A., Jessell, T.M., Wichterle, H. and Przedborski, S. (2007) Astrocytes expressing

ALS-linked mutated SOD1 release factors selectively toxic to motor neurons. *Nat. Neurosci.*, **10**, 615–622.

18. Boillée, S., Yamanaka, K., Lobsiger, C.S., Copeland, N.G., Jenkins, N.A., Kassiotis, G., Kollias, G. and Cleveland, D.W. (2006) Onset and progression in inherited ALS determined by motor neurons and microglia. *Science*, **312**, 1389–1392.

19. Beers, D.R., Henkel, J.S., Xiao, Q., Zhao, W., Wang, J., Yen, A.A., Siklos, L., McKercher, S.R. and Appel, S.H. (2006) Wild-type microglia extend survival in PU.1 knockout mice with familial amyotrophic lateral sclerosis. *Proc. Natl Acad. Sci. USA*, **103**, 16021–16026.

20. Xiao, Q., Zhao, W., Beers, D.R., Yen, A.A., Xie, W., Henkel, J.S. and Appel, S.H. (2007) Mutant SOD1^{G93A} microglia are more neurotoxic relative to wild-type microglia. *J. Neurochem.*, **102**, 2008–2019.

21. Clement, A.M., Nguyen, M.D., Roberts, E.A., Garcia, M.L., Boillée, S., Rule, M., MaMahon, A.P., Doucette, W., Siwek, D., Ferrante, R.J. *et al.* (2003) Wild-type nonneuronal cells extend survival of SOD1 mutant motor neurons in ALS mice. *Science*, **302**, 113–117.

22. Martin, L.J. and Liu, Z. (2007) Adult olfactory bulb neural precursor cell grafts provide temporary protection from motor neuron degeneration, improve motor function, and extend survival in amyotrophic lateral sclerosis. *J. Neuropathol. Exp. Neurol.*, **66**, 1002–1018.

23. Gowing, G., Philips, T., Van Wijmeersch, B., Audet, J.-N., Dewil, M., Van Den Bosch, L., Billiau, A.D., Robberecht, W. and Julien, P. (2008) Ablation of proliferating microglia does not affect motor neuron degeneration in amyotrophic lateral sclerosis caused by mutant superoxide dismutase. *J. Neurosci.*, **28**, 10234–10244.

24. Cova, E., Cereda, C., Galli, A., Cyrti, D., Finotti, C., Di Poto, C., Corato, M., Mazzini, G. and Ceroni, M. (2006) Modified expression of Bcl-2 and SOD1 proteins in lymphocytes from sporadic ALS patients. *Neurosci. Lett.*, **399**, 186–190.

25. Aguirre, T., Van Den Bosch, L., Goetschalckx, K., Tilkin, P., Mathijs, G., Cassiman, J.J. and Robberecht, W. (1998) Increased sensitivity of fibroblasts from amyotrophic lateral sclerosis patients to oxidative stress. *Ann. Neurol.*, **43**, 452–457.

26. McEachern, G., Kassovska-Bratinova, S., Raha, S., Tarnopolsky, M.A., Turnbull, J., Bourgeois, J. and Robinson, B. (2000) Manganese superoxide dismutase levels are elevated in a proportion of amyotrophic lateral sclerosis patient cell lines. *Biochem. Biophys. Res. Comm.*, **273**, 359–363.

27. Wiedemann, F.R., Winkler, K., Kuznetsov, A.V., Bartels, C., Vielhaber, S., Feistner, H. and Kunz, W.S. (1998) Impairment of mitochondrial function in skeletal muscle of patients with amyotrophic lateral sclerosis. *J. Neurol. Sci.*, **156**, 65–72.

28. Dupuis, L., Gonzalez de Aguilar, J.-L., Echaniz-Laguna, A. and Loeffler, J.-P. (2006) Mitochondrial dysfunction in amyotrophic lateral sclerosis also affects skeletal muscle. *Muscle Nerve*, **34**, 253–254.

29. Vielhaber, S., Winkler, K., Kirches, E., Kunz, D., Büchner, M., Feistner, H., Elger, C.E., Ludolph, A.C., Riepe, M.W. and Kunz, W.S. (1999) Visualization of defective mitochondrial function in skeletal muscle fibers of patients with sporadic amyotrophic lateral sclerosis. *J. Neurol. Sci.*, **169**, 133–139.

30. Krasnianski, A., Deschauer, M., Neudecker, S., Gellerich, F.N., Müller, T., Schoser, B., Krasnianski, M. and Zierz, S. (2005) Mitochondrial changes in skeletal muscle in amyotrophic lateral sclerosis and other neurogenic atrophies. *Brain*, **128**, 1870–1876.

31. Echaniz-Laguna, A., Zoll, J., Ponsot, E., N'Guessan, B., Tranchant, C., Loeffler, J.-P. and Lampert, E. (2006) Muscular mitochondrial function in amyotrophic lateral sclerosis is progressively altered as the disease develops: a temporal study in man. *Exp. Neurol.*, **198**, 25–30.

32. Comi, G.P., Bordoni, A., Salani, S., Franceschina, L., Sciacco, M., Prelle, A., Fortunato, F., Zeviani, M., Napoli, L., Bresolin, N. *et al.* (1998) Cytochrome c oxidase subunit I microdeletion in a patient with motor neuron disease. *Ann. Neurol.*, **43**, 110–116.

33. Corti, S., Donadoni, C., Ronchi, D., Bordoni, A., Fortunato, F., Santoro, D., Del Bo, R., Luccini, V., Crugnola, V., Papadimitriou, D. *et al.* (2009) Amyotrophic lateral sclerosis linked to a novel *SOD1* mutation with muscle mitochondrial dysfunction. *J. Neurosci.*, **276**, 170–174.

34. Derave, W., Van Den Bosch, L., Lemmens, G., Eijnde, B.O., Robberecht, W. and Hespel, P. (2003) Skeletal muscle properties in a transgenic mouse model for amyotrophic lateral sclerosis: effects of creatine treatment. *Neurobiol. Dis.*, **13**, 264–272.

35. Dupuis, L., Oubart, H., René, F., Gonzalez de Aguilar, J.-L. and Loeffler, P. (2004) Evidence for defective energy homeostasis in amyotrophic

36. Mahoney, D.J., Kaczor, J.J., Bourgeois, J., Yasuda, N. and Tarnopolsky, M.A. (2006) Oxidative stress and antioxidant enzyme upregulation in SOD1-G93A mouse skeletal muscle. *Muscle Nerve*, **33**, 809–816.

37. Schoser, B.G.H., Wehling, S. and Blottner, D. (2001) Cell death and apoptosis-related proteins in muscle biopsies of sporadic amyotrophic lateral sclerosis and polyneuropathy. *Muscle Nerve*, **24**, 1083–1089.

38. Atkin, J.D., Scott, R.L., West, J.M., Lopes, E., Quah, A.K.J. and Cheema, S.S. (2005) Properties of slow- and fast-twitch muscle fibers in a mouse model of amyotrophic lateral sclerosis. *Neuromuscul. Disord.*, **15**, 377–388.

39. Schaefer, A.M., Sanes, J.R. and Lichtman, J.W. (2005) A compensatory subpopulation of motor neurons in a mouse model of amyotrophic lateral sclerosis. *J. Comp. Neurol.*, **490**, 209–219.

40. Friese, A., Kaltschmidt, J.A., Ladle, D.R., Sigrist, M., Jessell, T.M. and Arber, S. (2009) Gamma and alpha motor neurons distinguished by expression of transcription factor Err3. *Proc. Natl Acad. Sci. USA*, **106**, 13588–13593.

41. Martin, L.J., Al-Abdulla, N.A., Brambrink, A.M., Kirsch, J.R., Sieber, F.E. and Portera-Cailiau, C. (1998) Neurodegeneration in excitotoxicity, global cerebral ischemia, and target deprivation: a perspective on the contributions of apoptosis and necrosis. *Brain Res. Bull.*, **46**, 281–309.

42. Weber, U.J., Bock, T., Buschard, K. and Pakkenberg, B. (1997) Total number and size distribution of motor neurons in the spinal cord of normal and EMC-virus infected mice—a stereological study. *J. Anat.*, **191**, 347–353.

43. Martin, L.J., Liu, Z., Chen, K., Price, A.C., Pan, Y., Swaby, J.A. and Golden, W.C. (2007) Motor neuron degeneration in ALS mutant superoxide dismutase-1 transgenic mice: mechanisms of mitochondriopathy and cell death. *J. Comp. Neurol.*, **500**, 20–46.

44. Martin, L.J., Gertz, B., Pan, Y., Price, A.C., Molkentin, J.D. and Chang, Q. (2009) The mitochondrial permeability transition pore in motor neurons: involvement in the patholbiology of ALS mice. *J. Exp. Neurol.*, **218**, 333–346.

45. Gurney, M.E., Pu, H., Chiu, A.Y., Dal Canto, M.C., Polchow, C.Y., Alexander, D.D., Caliendo, J., Hentati, A., Kwon, Y.W., Deng, H.X. *et al.* (1994) Motor neuron degeneration in mice that express a human Cu,Zn superoxide dismutase mutation. *Science*, **264**, 1772–1775.

46. Dobrowolny, G., Aucello, M., Rizzuto, E., Beccaficao, S., Mammucari, C., Bonconpagni, S., Belia, S., Wannenes, F., Nicoletti, C., Del Prete, Z. *et al.* (2008) Skeletal muscle is a primary target of SOD1^{G93A}-mediated toxicity. *Cell Metab.*, **8**, 425–436.

47. Yarom, R., Sapoznikov, D., Havivi, Y., Avraham, K.B., Schickler, M. and Groner, Y. (1988) Premature aging changes in neuromuscular junctions of transgenic mice with an extra human CuZnSOD gene: a model for tongue pathology in Down's syndrome. *J. Neurol. Sci.*, **88**, 41–53.

48. Avraham, K.B., Schickler, M., Sapoznikov, D., Yarom, R. and Yoram, G. (1988) Down's syndrome: abnormal neuromuscular junction in tongue of transgenic mice with elevated levels of human Cu/Zn-superoxide dismutase. *Cell*, **54**, 823–829.

49. Rando, T.A., Crowley, R.S., Carlson, E.J., Epstein, C.J. and Mohapatra, P.K. (1998) Overexpression of copper/zinc superoxide dismutase: a novel cause of murine muscular dystrophy. *Ann. Neurol.*, **44**, 381–386.

50. Kotulska, K., LePecheur, M., Marcol, W., Lewin-Kowalik, J., Larysz-Brysz, M., Paly, E., Matuszek, I. and London, J. (2006) Overexpression of copper/zinc-superoxide dismutase in transgenic mice markedly impairs regeneration and increase development of neuropathic pain after sciatic nerve injury. *J. Neurosci. Res.*, **84**, 1091–1097.

51. Bar-Peled, O., Korkotian, E., Segal, M. and Groner, Y. (1996) Constitutive overexpression of Cu/Zn superoxide dismutase exacerbates kainic acid-induced apoptosis of transgenic-Cu/Zn superoxide dismutase neurons. *Proc. Natl Acad. Sci. USA*, **93**, 8530–8535.

52. Estévez, A.G., Crow, J.P., Sampson, J.B., Reiter, C., Zhuang, Y., Richardson, G.J., Tarpey, M.M., Barbeito, L. and Beckman, J.S. (1999) Induction of nitric oxide-dependent apoptosis in motor neurons by zinc-deficient superoxide dismutase. *Science*, **286**, 2498–2500.

53. Zhou, J., Yi, J., Fu, R., Liu, E., Siddique, T., Rios, E. and Deng, X. (2010) Hyperactive intracellular calcium signaling associated with localized mitochondrial defects in skeletal muscle of an animal model of amyotrophic lateral sclerosis. *J. Biol. Chem.*, **285**, 705–712.

54. Muller, F.L., Song, W., Jang, Y.C., Liu, Y., Sabria, Y., Richardson, A. and Van Remmen, H. (2007) Denervation-induced skeletal muscle atrophy is associated with increased mitochondrial ROS production. *Am. J. Physiol. Regul. Integr. Comp. Physiol.*, **293**, R1159–R1168.

55. Fischer, L.R., Culver, D.G., Tennant, P., Davis, A.A., Wang, M., Castellano-Sanchez, A., Polak, M.A. and Glass, J.D. (2004) Amyotrophic lateral sclerosis is a distal axonopathy: evidence in mice and man. *Exp. Neurol.*, **185**, 232–240.

56. Pun, S., Santos, A.F., Saxena, S., Xu, L. and Caroni, P. (2006) Selective vulnerability and pruning of phasic motoneuron axons in motoneuron disease alleviated by CNTF. *Nat. Neurosci.*, **3**, 408–419.

57. Dobrowolny, G., Giacinti, C., Pelosi, L., Nicoletti, C., Winn, N., Barberi, L., Molinaros, M., Rosenthal, N. and Musarò, A. (2005) Muscle expression of a local Igf-1 isoform protects motor neurons in an ALS mouse model. *J. Cell Biol.*, **168**, 193–199.

58. Miller, T.M., Kim, S.H., Yamanaka, K., Hester, M., Umapathi, P., Arnson, H., Rizo, L., Mendell, J.R., Gage, F.H., Cleveland, D.W. *et al.* (2006) Gene transfer demonstrates that muscle is not a primary target for non-cell-autonomous toxicity in familial amyotrophic lateral sclerosis. *Proc. Natl Acad. Sci. USA*, **103**, 19546–19551.

59. Dupuis, L., Gonzalez de Aguilar, J.-L., Echaniz-Laguna, A., Eschbach, J., Rene, F., Oudart, H., Halter, B., Huze, C., Schaefer, L., Bouillard, F. *et al.* (2009) Muscle mitochondrial uncoupling dismantles neuromuscular junction and triggers distal degeneration of motor neurons. *PLoS One*, **4**, e5390.

60. Chen, K., Nothington, F.J. and Martin, L.J. (2009) Inducible nitric oxide synthase is present in motor neuron mitochondria and Schwann cells and contributes to disease mechanisms in ALS mice. *Brain Struct. Funct.*, doi:10.1007/s00429-009-0226-4.

61. Martin, L.J. (1999) Neuronal death in amyotrophic lateral sclerosis is apoptosis: possible contribution of a programmed cell death mechanism. *J. Neuropathol. Exp. Neurol.*, **58**, 459–471.

62. Martin, L.J. (2010) The mitochondrial permeability transition pore: a molecular target for amyotrophic lateral sclerosis. *Biochim. Biophys. Acta*, **1802**, 186–197.

63. Oppenheim, R.W. (1996) Neurotrophic survival molecules for motoneurons: a embarrassment of riches. *Neuron*, **17**, 195–197.

64. Martin, L.J., Chen, K. and Liu, Z. (2005) Adult motor neuron apoptosis is mediated by nitric oxide and Fas death receptor linked by DNA damage and p53 activation. *J. Neurosci.*, **25**, 6449–6459.

65. Martin, L.J., Pan, Y., Price, A.C., Sterling, W., Copeland, N.G., Jenkins, N.A., Price, D.L. and Lee, M.K. (2006) Parkinson's disease alpha-synuclein transgenic mice develop neuronal mitochondrial degeneration and cell death. *J. Neurosci.*, **26**, 41–50.

66. Laird, L.M., Farah, M.H., Ackerley, S., Hoke, A., Maragakis, N., Rothstein, J.D., Griffin, J., Price, D.L., Martin, L.J. and Wong, P.C. (2008) Motor neuron disease occurring in a mutant dynactin mouse model is characterized by defects in vesticular trafficking. *J. Neurosci.*, **28**, 1997–2005.

67. Chargé, S.B.P. and Rudnicki, M.A. (2004) Cellular and molecular regulation of muscle regeneration. *Physiol. Rev.*, **84**, 209–238.

68. Petropoulos, C.J., Rosenberg, M.P., Jenkins, N.A., Copeland, N.G. and Hughes, S.H. (1989) The chicken skeletal muscle α-actin promoter is tissue specific in transgenic mice. *Mol. Cell Biol.*, **9**, 3785–3792.

69. Martin, L.J., Price, A.C., McClendon, K.B., Al-Abdulla, N.A., Subramaniam, J.R., Wong, P.C. and Liu, Z. (2003) Early events of target deprivation/axotomy-induced neuronal apoptosis *in vivo*: oxidative stress, DNA damage, p53 phosphorylation and subcellular redistribution of death proteins. *J. Neurochem.*, **85**, 234–247.

70. Martin, L.J., Sieber, F. and Traystman, R.J. (2000) Apoptosis and necrosis occur in separate neuronal populations in hippocampus and cerebellum after ischemia and are associated with differential alterations in metabotropic glutamate receptor signaling pathways. *J. Cereb. Blood Flow Metab.*, **20**, 153–167.

71. Chayen, J., Bitensky, L. and Butcher, R.G. (1973) *Practical Histochemistry*. John Wiley & Sons, London.

72. Martin, L.J., Doebler, J.A. and Anthony, A. (1986) Cytophotometric analysis of neuronal chromatin and RNA changes in oxotremorine-treated rats. *Proc. Soc. Exp. Biol. Med.*, **181**, 41–48.

73. Shaikh, A.Y. and Martin, L.J. (2002) DNA base-excision repair enzyme apurinic/apyrimidinic endonuclease/redox factor-1 is increased and competent in the brain and spinal cord of individuals with amyotrophic lateral schlerosis. *Neuromolecular Med.*, **2**, 47–60.

74. Chang, C.C. (1999) Looking back on the discovery of alpha-bungarotoxin. *J. Biomed. Sci.*, **6**, 368–375.